J. Fluid Mech. (1987), *vol.* 182, *pp.* 255–290
Printed in Great Britain

The growth and breakdown of streamwise vortices in the presence of a wall

By JERRY D. SWEARINGEN AND RON F. BLACKWELDER
Department of Aerospace Engineering, University of Southern California, Los Angeles, CA 90089, USA

(Received 15 May 1986 and in revised form 22 January 1987)

The growth, breakdown, and transition to turbulence of counter-rotating streamwise vortices, generated via a Görtler instability mechanism, was used to experimentally model the eddy structures found in transitional and turbulent flat-plate boundary layers. The naturally occurring vortices have been studied using smoke-wire visualization and multiple-probe hot-wire rakes. Results show that low-speed regions are formed between the vortices as low-momentum fluid is removed away from the wall. The low-speed regions grow in the normal direction faster than a nominally Blasius boundary layer and create strongly inflexional normal and spanwise profiles of the streamwise velocity component. Instability oscillations develop on these unstable profiles that scale with the local shear-layer thickness and velocity difference. Contrary to expectations however, the spatial scales of the temporal velocity fluctuations correlate better with the velocity gradient in the spanwise direction than with the normal velocity gradient. The nonlinear growth of the oscillations is quite rapid and breakdown into turbulence occurs within a short timescale.

1. Introduction

Most bounded transitional and turbulent shear flows are known to have deterministic eddy structures that govern their dynamics. In transitional flows, these eddies often develop as the result of an instability and play a major role in the breakdown of the laminar state. In turbulent flow fields, they are responsible for the turbulent energy production. One of the most prevalent eddy structures found in both transitional and turbulent bounded shear flows is counter-rotating streamwise vortices. The present investigation was undertaken to study the dynamics governing the growth, breakdown, and transition to turbulence of streamwise vortices.

Klebanoff, Tidstrom & Sargent (1962) among others have shown that although the Tollmien–Schlichting wave solutions of the Orr–Sommerfeld equation adequately describe the initial instability in boundary layers undergoing transition, a growing three-dimensional disturbance rapidly develops which is best described as counter-rotating streamwise vortices. Most significantly, these vortices pumped low-speed fluid between them and away from the wall which led to an inflexional velocity profile that subsequently developed into another localized instability. This latter instability was manifested by a velocity 'spike' followed by breakdown into turbulence. More recently, Nishioka, Asai & Iida (1980) have shown that a comparable eddy structure exists in transitional channel flows.

Cantwell, Coles & Dimotakis (1978) using the aluminium-flake visualization technique observed elongated streamwise disturbances in the wall region of growing turbulent spots. They conjectured that these were a manifestation of Taylor–Görtler

vortices generated by the passage of the spot. Haritonidis (1978) concluded from hot-wire-rake measurements on the spot centreline that the velocity field is consistent with the conjectured streamwise vortices of Cantwell *et al.* and that the qualitative spot features (i.e. spanwise streak spacing etc.) were the same.

Turbulent boundary layers are known to consist of two different sets of coherent eddies which appear randomly in space and time. In the outer flow, a large-scale structure controls the entrainment of non-turbulent fluid into the boundary layer while the inner near-wall flow is governed by eddy structures that appear to be quite similar to those described above for transitional flows. The wall eddies are involved in a sequence of events termed the 'bursting process' that are responsible for 70–90 % of the turbulent energy production and the concomitant solid-boundary drag. Kline *et al.* (1967) have shown that this eddy structure begins with the formation of elongated regions of low-speed fluid approximately $\Delta z^+ = 20$ wide and $\Delta x^+ > 1000$ long where x^+ and z^+ are the streamwise and spanwise coordinates non-dimensionalized with the wall variables consisting of the friction velocity u_τ, and the kinematic viscosity ν. A number of authors, including Bakewell & Lumley (1967) for a turbulent pipe flow, Blackwelder & Eckelmann (1979) for a channel flow, and Smith & Schwartz (1983) for a flat-plate turbulent boundary layer, have shown that these streaks are consistent with low-speed fluid being removed from the wall by pairs of counter-rotating streamwise vortices having a spanwise wavelength of $\lambda^+ \approx 100$. Coles (see Cantwell *et al.*) and others have suggested that these vortices may be due to a Taylor–Görtler instability resulting from streamwise curvature imposed by the large-scale outer structure. Once formed, two counter-rotating vortices act to pump low-speed fluid away from the wall, thus forming the low-speed streaks and a consequent inflexional velocity profile as measured by Blackwelder & Kaplan (1976). This leads to an instability similar to the type found in transitional boundary layers. Oscillations associated with this instability terminate in a rapid ejection of fluid away from the wall which subsequently interacts with outer fluid in an intense, chaotic motion. The rapid timescale of this motion led Kline *et al.* (1967) to call it a burst; subsequent authors have referred to the entire process as the bursting phenomenon. These events have been discussed in detail by numerous authors including Kim, Kline & Reynolds (1971) and Corino & Brodkey (1969).

Several authors have suggested similarities between the eddies described for the transitional and turbulent flow fields. Blackwelder (1983) has summarized much of the available data for boundary layers and compares the constituent elements of the eddy structures for both these flow regimes. He reiterates the importance of counter-rotating streamwise vortices in the overall sequence of events and suggests that not only are the dynamics of the vortices similar, but that their dimensions are comparable when scaled with the viscous parameters, ν and u_τ. One of the suggestions arising from the Workshop on Coherent Structure of Turbulent Boundary Layers (Smith & Abbott 1978) was that the dynamics of counter-rotating vortices should be the subject of a detailed study. Furthermore, Morkovin (1979) underlined the need for reliable experimental studies to aid efforts to establish a theoretical description of streamwise vortices as they evolve, and transition in laminar boundary layers. Several studies have pursued this course of investigation; however they have met with limited success in actually describing the vortex dynamics due to experimental constraints. In turbulent boundary layers, the streamwise vortices appear randomly in space and time making their study extremely difficult. In transitional boundary layers on flat plates, the physical dimensions of the vortices are quite small and they are associated with and modulated by the Tollmien–Schlichting waves; hence

difficulty arises in separating the two effects. Thus, the situation remains that there is little information available explaining the dynamics of the growth and breakdown of streamwise vortices.

Evidence from an experimental study by Bippes (1972) indicates that the growth and breakdown of streamwise vortices generated on a concave wall via the Görtler instability mechanism are quite similar to those found in the transitional and turbulent flow fields previously mentioned. The analogy between these flow fields has been exploited in the study described here. Specifically, streamwise vortices generated by the Görtler instability have been used to model the growth and breakdown of counter-rotating vortices in transitional and turbulent boundary layers. Streamwise vortices generated in this way have a number of important advantages that make their study easier: (i) their physical scales are much larger; (ii) they occur in a laminar environment; (iii) they are steady in the time domain (i.e. no background turbulent fluctuations or Tollmien–Schlichting waves); and (iv) their originating mechanism as well as point of origin is known.

2. Experimental apparatus

2.1. *Wind tunnel*

The experiments were conducted in a low-speed, open-return wind tunnel specially designed so the laminar boundary layer generated would become unstable to a Görtler instability earlier than to the Tollmien–Schlichting instability. The facility is shown schematically in figure 1. The flow is generated at the upstream end of the wind tunnel by a 75 cm diameter vane axial fan powered by a five horsepower variable speed d.c. motor. Velocity stability of this configuration is better than 1 % throughout its speed range. Filtering of the incoming air stream is provided by a screen and stilling box at the upstream entrance to the fan. A 130 cm long paraboloid-shaped tail cone is attached to the downstream end of the fan hub assembly to ensure that a reasonably uniform flow enters the diffuser section. To prevent transmission of vibration caused by residual fan-blade unbalance, the fan section is isolated from the rest of the tunnel by a rubber boot.

A $5\frac{1}{2}^\circ$ diffuser section of length 488 cm connects the fan assembly with a 122 cm × 122 cm stilling chamber. To ensure that no separation occurs in the diffuser section, 15 mesh, 77 % porosity fibreglass screens are placed at 130 cm intervals throughout its length. The stilling chamber contains a honeycomb and four fine-mesh screens to establish the flow direction and control the turbulence level. The aluminium honeycomb has cells 10 cm in length and 1 cm in diameter. The four screen panels are made of 40 mesh woven stainless-steel cloth with 72 % porosity and follow the honeycomb section at 20 cm intervals.

Downstream of the stilling chamber a two-dimensional 8:1 contraction section accelerates the flow to the required test-section velocity. The contraction fairing, which begins 30 cm past the last stilling-chamber screen, follows a smooth fifth-order polynomial curve and reduces the flow area to 122 cm × 18 cm at its exit. The sidewall boundary layers are removed tangentially to the flow direction at the exit of the contraction through a 1.5 cm suction slot concentric with the leading edge of the test section as shown in figure 1. This provides a distinct origin for the boundary-layer flow in the test section and is accomplished using a low-pressure plenum chamber surrounding the slot and connected to two auxiliary axial blowers. The blowers can be adjusted independently to accurately control the flow rate from the plenum and thus from the slot.

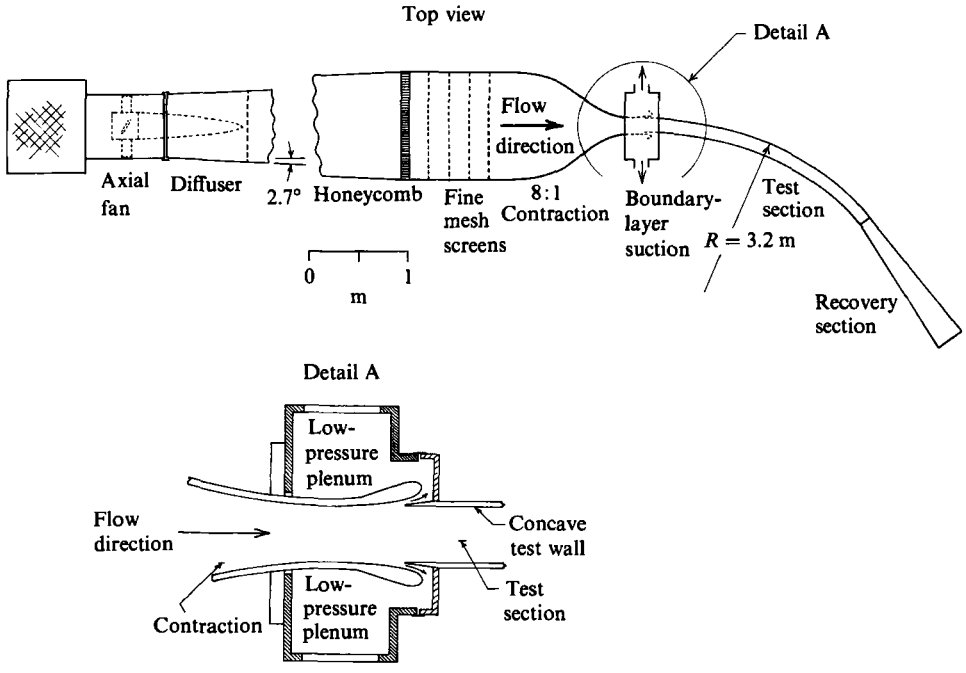

FIGURE 1. Schematic of the curved-test-section wind-tunnel facility.

The curved portions of the test rig were fabricated from Plexiglas. The end result is a curved test section 244 cm long with a 120 cm × 15 cm cross-section and a 320 cm radius of curvature supported in a rigid steel reinforcing frame. A 183 cm long recovery section follows the test section to minimize propagation of outlet separation disturbances upstream into the test flow. The concave working surface has a circular leading edge which coincides with the origin of the streamwise coordinate x. The y-axis is taken as the normal to this wall and the transverse coordinate is labelled z with its origin arbitrarily located near midspan. The opposite convex wall consists of a series of moveable panels of constant curvature spanning the test section. The streamwise length of these panels varies from 10 cm to 122 cm and thus their relative placement is used to coarsely position a two-dimensional (y and z) traversing section at different downstream locations. Precise streamwise positioning is accomplished using an adjustable probe support attached to the y- and z-traverse assembly.

Measurements of the streamwise static-pressure distribution show C_p deviation along the test section centreline to be less than 5% for free-stream velocities in the range 2.5 to 10 m/s. Spanwise traverses of the free-stream velocity show deviations of less than 0.5% across the test section exclusive of top and bottom wall boundary layers. The free-stream turbulence level is less than 0.07% for all velocities.

2.2. *Instrumentation*

Constant-temperature hot-wire anemometers were the primary tool for data acquisition in this study. The anemometer circuit used is a modification of similar electronics described by Blackwelder & Kaplan (1976). Overheat ratios of nominally 20% were used throughout this investigation.

Two different hot-wire-rake configurations were employed to simultaneously measure the fluctuating streamwise velocity at a number of locations. The y-rake is

utilized to measure the normal distribution of streamwise velocity. The rake is the same as the one detailed in Wygnanski, Haritonidis & Kaplan (1979). Briefly the rake consists of 10 pairs of jeweller's broaches 1.1 mm apart and spaced approximately logarithmically in y. The sensor distances from the bottom of the rake (i.e. the wall also) are 1.0, 2.0, 3.0, 4.1, 6.1, 8.1, 11.2, 15.2, 19.3 and 25.4 mm. The z-rake, used to measure the spanwise distribution of streamwise velocity, has 12 individual sensor elements 0.5 mm long with a centre-to-centre separation of 1.5 mm. In all cases the sensor material used was 2.5 μm diameter platinum–10% rhodium wire which was soft soldered to the jewellers broaches.

Traverse control, data acquisition, and subsequent processing were performed with a Digital Equipment Corporation PDP-11/55 minicomputer using simple FORTRAN programs. The digitizing subsystem is capable of simultaneous data acquisition from one to sixteen channels through the use of individual sample-and-hold modules. Analog signals can be acquired with 12-bit resolution at an aggregate rate of 350000 samples per s. Double buffering in memory allows an aggregate throughput of 240 kilowords per s to either of two 67 Mbyte Winchester disks for further processing. Communication with the computer was through a Tektronix 4006-1 terminal which was also used to graphically display results.

3. Experimental procedures

3.1. *Flow-visualization technique*

The smoke-wire technique, originally developed by Tani & Sakagami (1962) and more recently utilized by Corke *et al.* (1980) and others, was employed to visually study the flow field. This method of visualization consists of resistively heating a fine wire that was previously coated with machine oil. The heating vaporizes the oil film which is consequently swept away by the flow and partially condensed as a highly visible white smoke sheet. The sheet actually consists of many fine smoke filaments (typically 1.5 mm apart) originating from discrete beads of oil which formed on the wire as the result of the Marangoni surface-tension effect.

The smoke-wire arrangement used in this study was similar to that employed by W. S. Saric (1980, private communication). A stainless-steel wire was mounted vertically between two support tubes extending into the test section through a movable Plexiglas panel on the opposite wall of the test section. The wire was oriented transverse to the flow direction and parallel to the working surface in order to visualize flow in the (x, z)-plane. The 100 μm diameter stainless wire used typically required 50–60 V d.c. to adequately heat its 60 cm length, depending on the local flow velocity and the desired duration and intensity of the smoke. A two-stage timing circuit was used to separately control the length of time the wire was heated and the time delay before photographic records of the smoke lines were made. Illumination along the spanwise axis was provided by a high-intensity stroboscope triggered by the camera lens. The 10 μs flash duration was adequate to freeze the motion under study.

3.2. *Hot-wire measurement techniques*

The frequency response of the constant-temperature hot-wire anemometers was adjusted prior to their static calibration and at the maximum velocity expected in the subsequent experiment. Using the familiar square-wave test, a frequency response typically greater than 10 kHz was achieved for the 2.5 μm diameter sensors

utilized. Static calibration of the hot wires was accomplished by operating them in the free stream of the wind tunnel over the range of velocities to be encountered within the boundary layer. The calibration procedure was the same as the one used by Blackwelder & Haritonidis (1983). Using this procedure, calibration of the multiple-sensor rakes required no more real time than that for a single sensor probe.

A typical experimental run commenced by calibrating the probe of choice in the tunnel free stream as previously described. Immediately following the calibration, the probe was appropriately positioned in the boundary layer and the desired data recorded. At the conclusion of the data acquisition, the probe was returned to the free stream and the calibration was checked. A drift of more than 2 % for any of the probe's sensors caused the data to be rejected and the calibration/data acquisition process to be repeated.

Measurements of the streamwise component of velocity were taken primarily in two ways. A single hot-wire probe was traversed (i.e. moved a small distance, data collected, and moved again) over a large spanwise distance to record the spatial variation in the mean streamwise velocity $U(z)$. To maintain the sensor at a constant elevation (fixed y/δ_{L}) at all spanwise positions, it was necessary to mount the probe on a streamlined sled riding on the working surface. The distance between the sensor and the wall was adjustable via a small screw and pivot incorporated in the sled.

The second major method used to study the streamwise velocity field was to traverse the y-rake previously described over a short spanwise distance in order to obtain $u(y, z, t)$. The rake was maintained at a constant height above the wall and measurements were taken at a number of spanwise locations, typically over a 3.2 cm span covering two pairs of counter-rotating streamwise vortices. This technique produced a grid of some 330 individual streamwise velocity measurements in the (y, z)-plane and was repeated at a number of streamwise positions. Similarly the z-rake was moved incrementally in the normal direction at a fixed x-location to obtain essentially the same information as with the y-rake; however, the y-rake method was normally utilized since a greater distance in the spanwise direction could be covered. The z-rake was used mainly in cases where simultaneous data in the spanwise direction were required.

4. Results

Görtler (1940) was the first to analyse the stability of flow over a concave wall. He showed that instability due to an inviscid centrifugal mechanism results in a system of counter-rotating vortices aligned in the flow direction. A sketch of these vortices is shown in figure 2. Their stability is governed by the Görtler parameter

$$G\ddot{o}_\theta = \frac{U_\infty \theta}{\nu}\left(\frac{\theta}{R}\right)^{\frac{1}{2}},$$

where θ is the momentum thickness and R is the radius of wall curvature. Hämmerlin (1955) and Smith (1955) subsequently confirmed Görtler's analysis that for $G\ddot{o}_\theta > 0.3$ streamwise vortices are unstable and grow in the downstream direction. Most of the measurements reported here were performed at $U_\infty = 5$ m/s, yielding $0.5 < G\ddot{o}_\theta < 10$, and $10^4 < Re_x < 4 \times 10^5$ for the streamwise positions explored. These conditions were chosen such that the boundary layer was stable with respect to Tollmien–Schlichting waves. In all cases the naturally occurring disturbances were used to generate the streamwise vortices, i.e. nothing was done to fix the spanwise

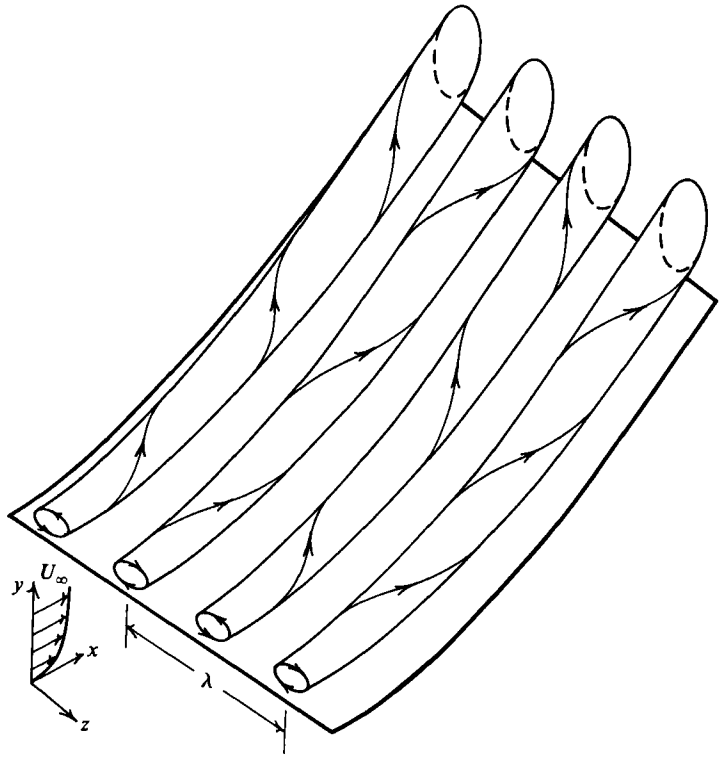

FIGURE 2. Sketch of the streamwise vortices developing on a concave wall owing to the Görtler instability mechanism.

wavelength or generate a disturbance field upstream of the leading edge. The coordinate system used for the various measurements is also given in figure 2.

4.1. *Flow visualization*

A smoke-wire visualization of the flow field showing a typical pattern in the (x, z)-plane is presented in figure 3. The grid lines shown are equally spaced 10 cm apart in both x and z and the numbers shown along the test-plate centreline measure the distance from the leading edge of the test plate. The smoke wire, located at $x = 21.5$ cm and $y/\delta_L = 0.3$, initially produced a series of fine smoke filaments spaced ≈ 1.5 mm apart which were convected downstream. They were rapidly coalesced into elongated streaks by the action of the longitudinal vortex field as seen in the photograph. Hot-wire measurements presented later show that the smoke-filled regions have a lower velocity than their surroundings, similar to the low-speed streaks observed in turbulent boundary layers. The Görtler number based on the Blasius momentum thickness varies from 5.6 to 8.6 as the flow moves from left to right in the photograph. The spanwise wavelength of the streak spacing is roughly 2.3 cm and appears to be independent of x. Thus the non-dimensional wavenumber $k\theta$ (using the Blasius θ-value) varies from 0.24 to 0.32 in the photograph. These values are in agreement with the stability analysis for the Görtler problem; i.e. they are located in the unstable region of the stability diagram.

Downstream, the streaks develop oscillations, seen for $x < 90$ cm, which ultimately

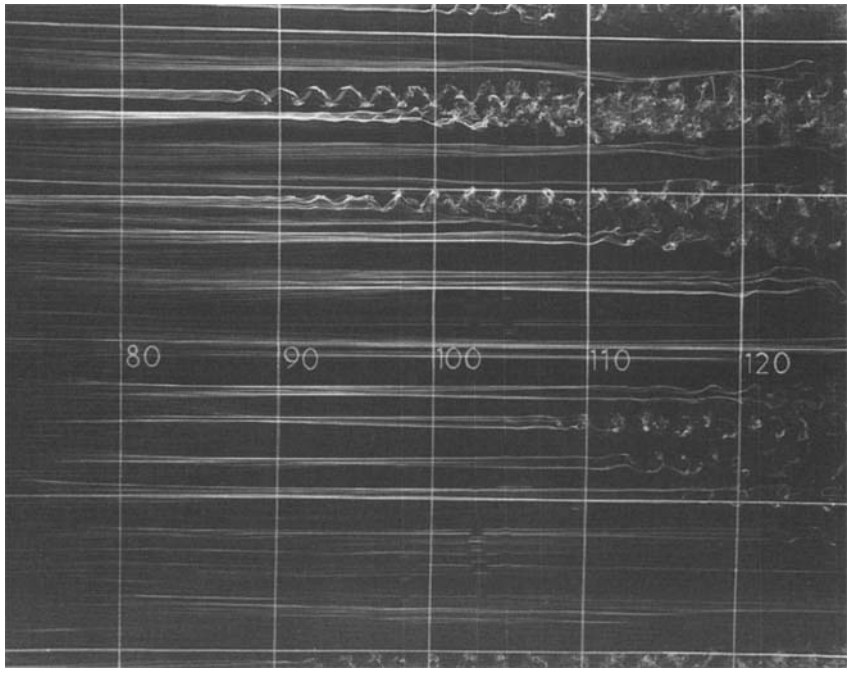

FIGURE 3. Instantaneous visualization of the flow field in the (x, z)-plane using a smoke wire at $x = 21.5$ cm and $y/\delta_L = 0.3$. Flow is from left to right and the grid spacings are 10 cm in both the streamwise and spanwise directions.

breakdown into turbulence. Breakdown occurs individually on each streak at a Görtler number between 6.7 and 9, corresponding approximately to the critical value of $G\ddot{o}_\theta = 9$ reported by Liepmann (1945) for transition due to streamwise vortices. Additionally, Dryden (1948) found that this value could vary in a range between 6 and 9 depending on the intensity of turbulence in the oncoming stream. Note that there is some irregularity in the spanwise spacing of the low-speed streaks, plus they appear to breakdown more or less independently of one another; i.e. at varying downstream locations. This seems to be the result of the random distribution and intensities of disturbances in the oncoming flow upstream of plate's leading edge. An examination of the flow-visualization photograph in figure 17 of Bippes (1972) for the naturally occurring disturbances in his concave-wall flow indicates a similar situation.

Additional realizations of the smoke-wire visualization show that the long-term similarity and repeatability of the phenomena under study is very good. The low-speed streaks and thus the streamwise vortices producing them remain fixed in preferred spanwise locations giving a reproducible pattern from realization to realization for a given wind-tunnel configuration. The particular spanwise pattern obtained was, however, found to depend strongly on the last screen in the wind-tunnel settling chamber (i.e. changing the screen order in the settling chamber or rotating the downstream screen by 90° altered the observed streak locations and pattern). The mean streak spacing, however, was found to remain essentially the same independent of screen geometry or tunnel configuration. These results are discussed more fully in Swearingen & Blackwelder (1986). In addition to the vortices remaining fixed in

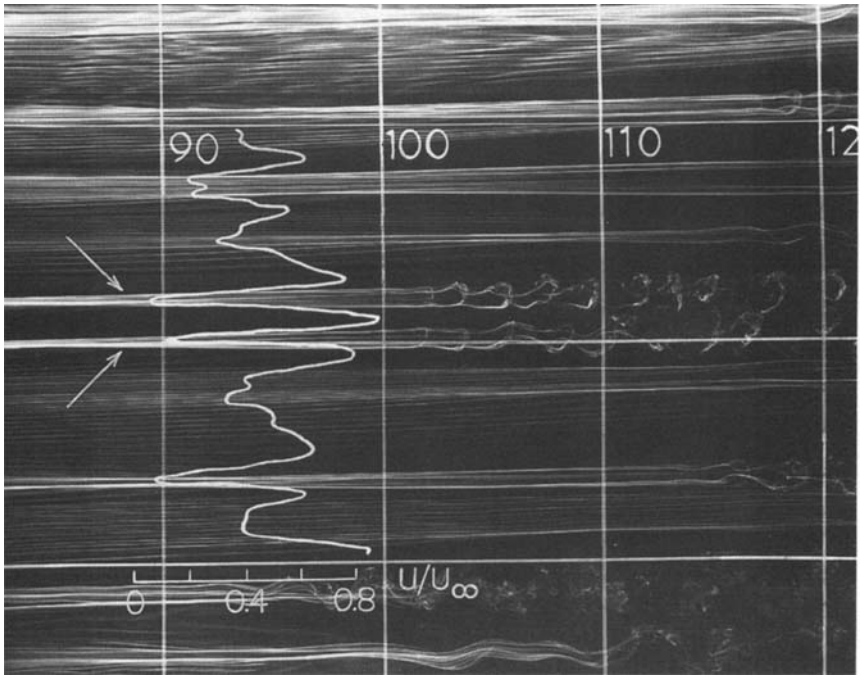

FIGURE 4. Spanwise variation of the mean streamwise velocity at $y/\delta_L = 0.25$ superimposed on a flow-visualization realization.

space, the individual streaks breakdown at more or less the same x-location from one realization to the next.

An important result noticeable from the visualization study is that the eddy lengthscales in the Görtler flow are comparable with those in turbulent boundary layers when scaled with the friction velocity

$$u_\tau \equiv \left(\nu\left(\frac{\partial U}{\partial y}\right)_w\right)^{\frac{1}{2}},$$

and the kinematic viscosity ν, as suggested by Blackwelder (1983). In the case of the initially laminar Görtler flow u_τ is obtained from the Blasius profile. The spanwise spacing of the low-speed streaks in figure 3 is roughly $195\nu/u_\tau$ compared to the value of $100\nu/u_\tau$ most often quoted for turbulent boundary layers. The streamwise wavelength of the oscillations which ultimately result in turbulence is roughly $175\nu/u_\tau$ compared with 100–$200\nu/u_\tau$ reported for transitional and turbulent boundary layers on flat plates. Additionally the streamwise extent of the low-speed streaks in the photographs (several thousand viscous lengthscales) compares favourably with the observations that the streaks in turbulent boundary layers have lengths of typically $1000\nu/u_\tau$ or greater.

To verify that the smoke-filled regions of the previous visualizations indeed had a lower velocity than their surroundings, a hot wire was traversed in the spanwise direction at a fixed distance away from the wall. Figure 4 shows the spanwise variation of the mean streamwise velocity at $y/\delta_L = 0.25$ superimposed on a flow-visualization realization. Note that the mean velocity has been normalized with

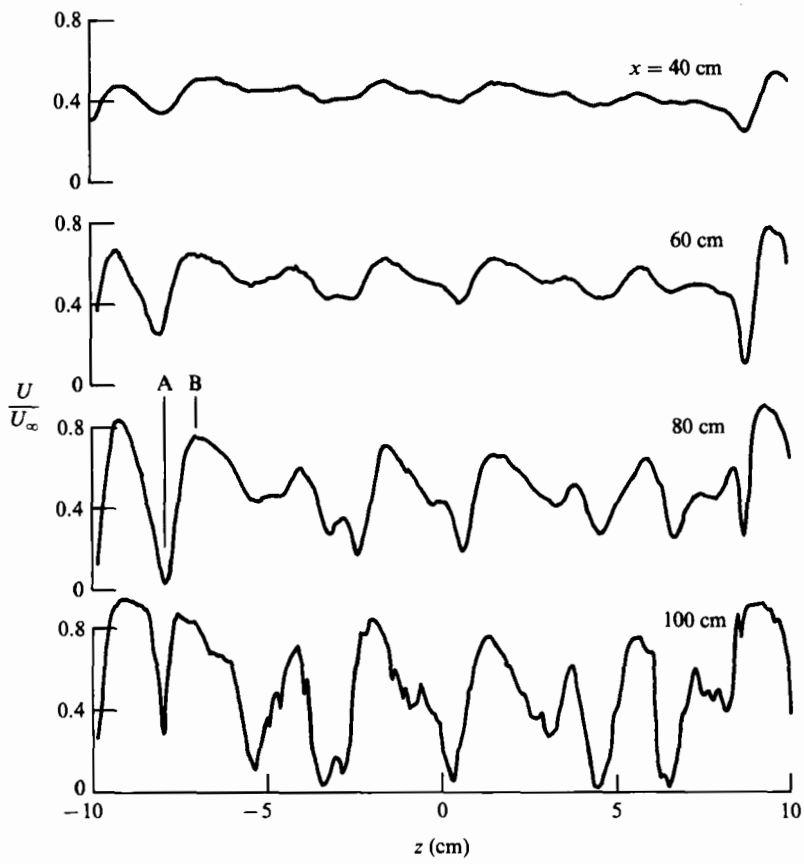

FIGURE 5. Spanwise distributions of the mean streamwise velocity at fixed $y/\delta_L = 0.25$. Sections A and B correspond to a peak and a valley respectively in the nomenclature of Klebanoff *et al.* (1962).

the free-stream velocity and that the streamwise placement of the velocity trace is arbitrary (the measurement location was actually $x = 82.5$ cm). The spanwise pattern is consistent with the expected longitudinal counter-rotating vortices that result from the destabilizing effects of curvature on the initially Blasius flow. The velocity field of the vortices induces a spanwise-periodic normal motion in the boundary layer such that alternating regions develop where low-momentum fluid is moved away from the wall and high-speed outer fluid is moved towards the wall, similar to that of Tani & Sakagami (1962).

The arrows noted on the photograph point out low-speed regions that will be investigated in more detail later.

4.2. *Comparison with linear Görtler theory*

Spanwise distributions of the mean streamwise velocity component as in the previous figure were made for several downstream positions. Figure 5 shows the typical development of the flow field with x and how the presence of the longitudinal vortices changes the mean flow within the boundary layer as they grow in amplitude. The period of amplitude growth is followed by saturation and eventual breakdown to turbulence in the vicinity of $x = 100$ cm. This can be seen clearly in the previous flow-visualization photographs and from temporal velocity traces to be presented

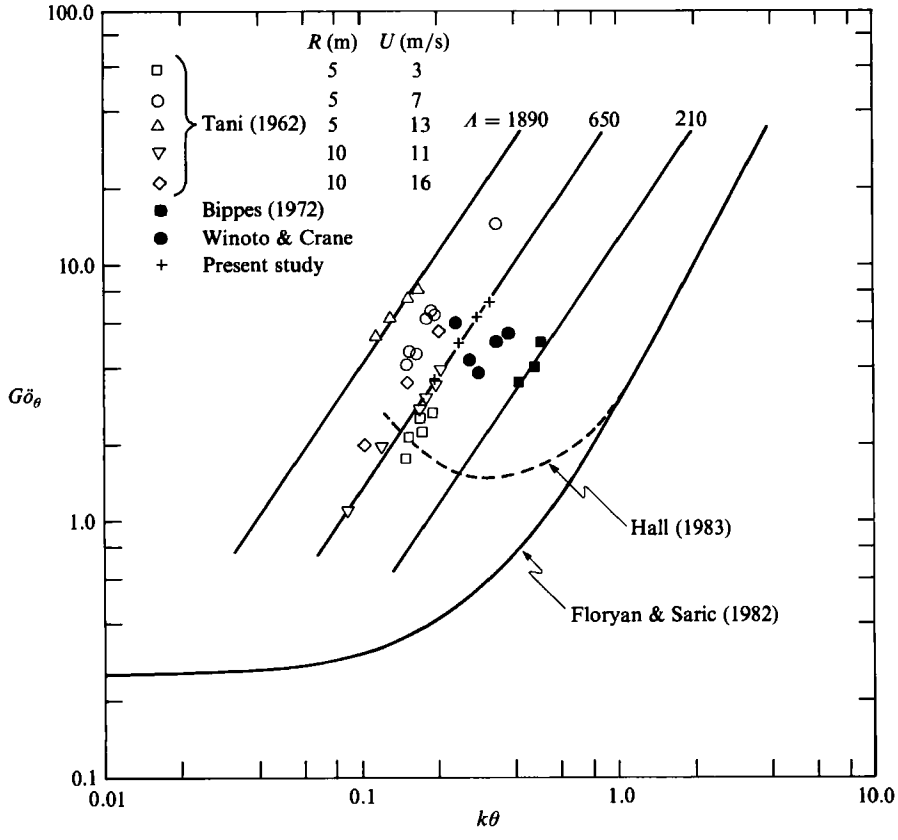

FIGURE 6. Comparison of available experimental data with the theoretical neutral stability limit.

later. Sections A and B are identified in the plot as corresponding to a peak and a valley respectively in the nomenclature of Klebanoff *et al.* (1962). A 'peak' is the location where $u'(z)$ is a maximum and $U(z)$ a minimum. These will be referred to below.

Velocity measurements such as those presented in figure 5 were used to determine the spanwise disturbance wavelength λ. Hand counting of peaks and valleys showed that the spanwise wavelength is roughly 2.3 cm, independent of streamwise location. Note that there was some difficulty associated with defining a spanwise wavelength due to ambiguity as to what constituted an actual peak or valley. This irregularity in the spanwise variation and the observation from the flow visualizations that the streaks breakdown independently illustrates the random nature of the disturbance field. For comparison, the data of figure 5 were studied using a maximum-entropy spectral analysis technique originally due to Burg (1967). An algorithm developed by Andersen (1974) was used to determine the spanwise wavelength from the data. This technique gave virtually the same estimate of the average wavelength as the visual identification of peaks and valleys. The wavelength determined in these two ways agreed well with that observed from the flow visualizations.

As mentioned earlier, the dimensional wavelength of the spanwise disturbance was found to be independent of downstream location. Additionally, a change in free-stream velocity over the range 2.5–10 m/s did not change the spanwise wavelength

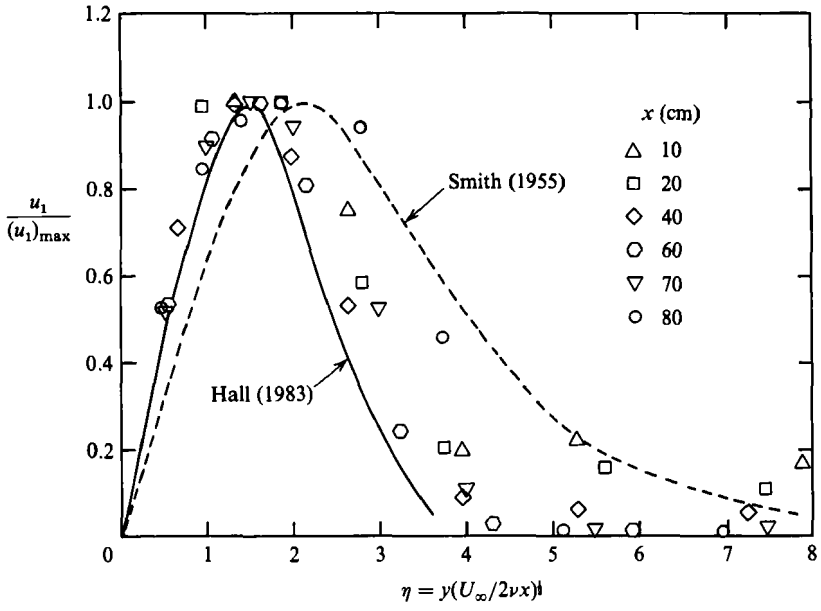

FIGURE 7. Comparison of the u-component of the disturbance velocity field with theoretical eigenfunctions.

substantially. These results are shown in the stability diagram of figure 6 by plotting the Görtler parameter $G\ddot{o}_\theta$ versus the non-dimensional wavenumber $k\theta$, where θ is the calculated momentum thickness of the Blasius boundary layer and $k = 2\pi/\lambda$ is the spanwise wavenumber. Note that the experimental points for a particular run (i.e. constant λ for a given set of conditions) establish lines of constant slope $\frac{3}{2}$ and thus a non-dimensional wavelength parameter can be defined:

$$\Lambda = \frac{U_\infty R}{\nu}(\lambda/R)^{\frac{3}{2}}.$$

This result is not unexpected since the wavenumber does not change and the Görtler parameter varies as $\theta^{\frac{3}{2}}$. The observed wavelength of 2.3 cm corresponds to $\Lambda \sim 670$. This is in good agreement with the results of Tani (1962) and Tani & Sakagami (1962).

In figure 6, comparison is made with several theoretical predictions of neutral stability for small-amplitude disturbances. The unique neutral curve of Floryan & Saric (1982) is presented along with one of the neutral curves due to Hall (1983) for a typical set of disturbance conditions (figure 7). Hall found the neutral stability limit to depend on the location and form of the initial perturbation. In the asymptotic limit of high wavenumber his prediction agrees quite well with that of Floryan & Saric. These analyses both differ from earlier works on the Görtler problem in that they solve the partial differential equations governing the linear stability of the flow employing *no* parallel-flow approximation. The use of a parallel-flow assumption presumably accounts for the disagreement between the early investigations over the low-wavenumber behaviour. Regardless of the neutral stability curve chosen, however, all of the experimental points lie in the region where an amplified disturbance is predicted.

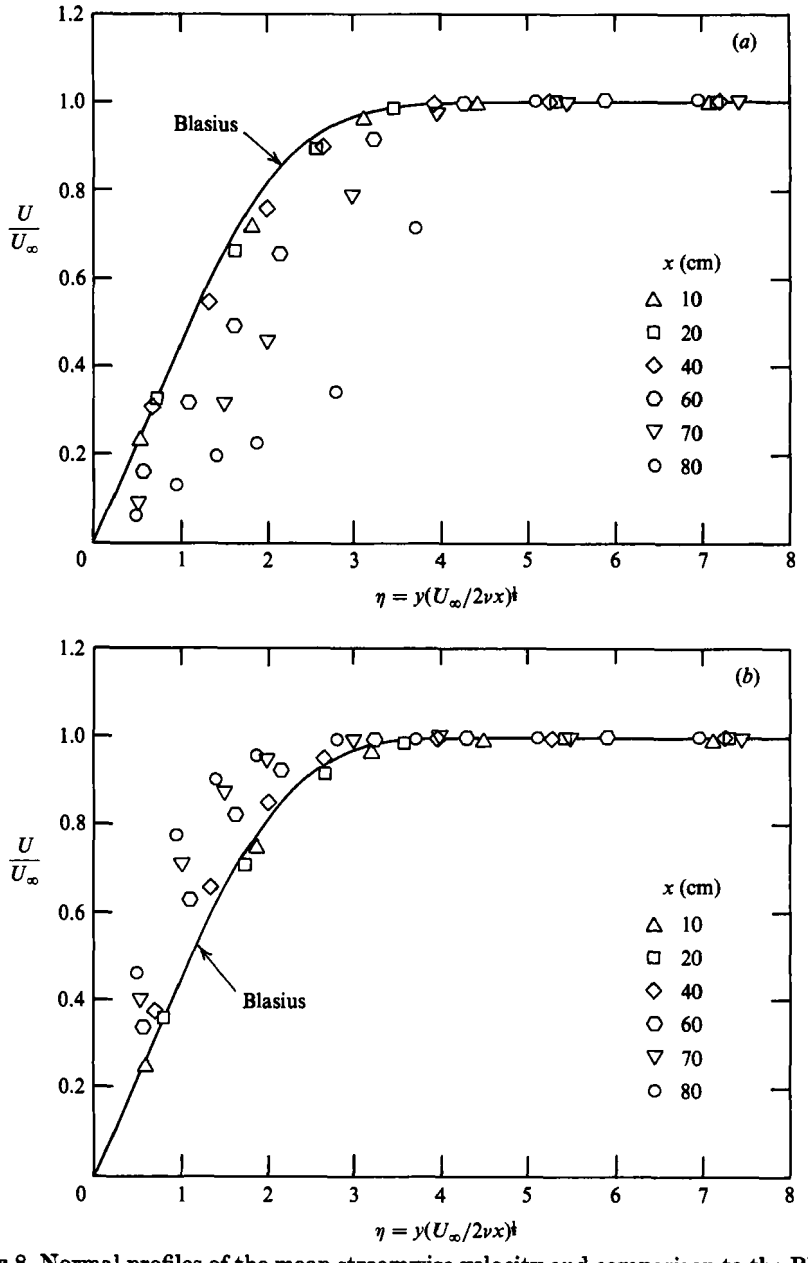

FIGURE 8. Normal profiles of the mean streamwise velocity and comparison to the Blasius solution for spanwise positions corresponding to (*a*) section A (a peak), (*b*) section B (a valley).

In the spatially developing small-disturbance theories, the streamwise velocity perturbation is of the form

$$U_1 \sim u_1(X, Y) \cos kZ,$$

where X, Y and Z are the typical dimensionless boundary-layer coordinates. Experimental data for the u-component of the disturbance velocity field $u_1/(u_1)_{\max}$ given in figure 7 show reasonable agreement with the theoretical eigenfunctions

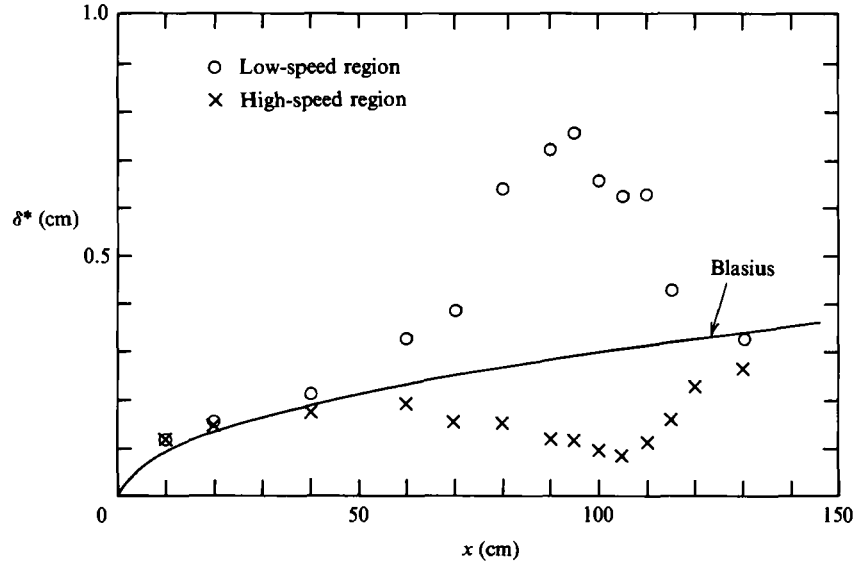

FIGURE 9. Downstream development of the displacement thickness in sections A (low-speed region) and B (high-speed region).

predicted by Hall (1983) and Smith (1955). Of note is the fact that the shape of this velocity distribution remains essentially unchanged with increasing downstream distance up to the measurement position where deviation would be expected owing to its proximity to transition. This is in qualitative agreement with the findings of Hall.

4.3. *Mean statistics*

Normal profiles of the mean streamwise velocity at six downstream locations are shown in figure 8 for spanwise positions corresponding to sections A and B in figure 5 (a peak and a valley respectively). Upstream of the $x = 40$ cm location the experimental data agree very well with the flat-plate Blasius solution in both sections A and B. By $x = 40$ cm in the downstream development, a noticeable distortion of the Blasius profile is apparent. Section A shows a defect in velocity from the Blasius flow while section B shows a corresponding increase in velocity. Distortion of the Blasius flow continues with increasing downstream distance producing concentrated regions of low- and high-speed fluid and giving the boundary layer a wavy appearance in the spanwise direction as its thickness alternately increases and decreases. Thus, across one spanwise wavelength, the streamwise velocity profile $U(z)$ is inflexional. In the low-speed region at $x = 80$ cm the mean profile becomes inflexional in the y-direction also. Both inflexional profiles indicate the imminent onset of another instability and breakdown to turbulence.

The measured development of the displacement thickness δ^* in the downstream direction for the low- and high-speed regions is compared with the Blasius growth in figure 9. In the low-speed region, δ^* increases dramatically beginning near $x = 40$ cm and continues until reaching a peak value at $x = 95$ cm. The corresponding displacement thickness in the high-speed region begins to decrease at $x = 40$ cm and reaches a minimum at about $x = 105$ cm. After reaching their extrema the displacement thicknesses in both high- and low-speed regions begin to rapidly equilibrate to the same value. The flow-visualization photographs and temporal

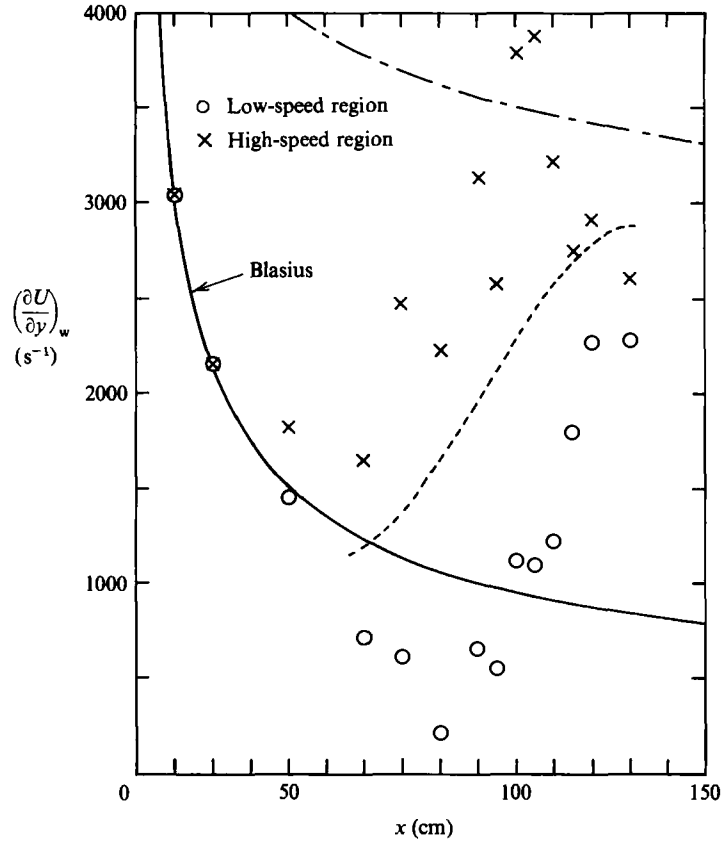

FIGURE 10. Downstream development of the wall shear in sections A (low-speed region) and B (high-speed region): ——, Blasius; —·—·, flat-plate turbulent boundary layer; – – – –, fit of average wall shear.

velocity traces presented later suggest that this is the result of the onset of turbulence and its consequent increased mixing smearing out the laminar spanwise structure.

Figure 10 shows the downstream development of the measured wall shear, $(\partial U/\partial y)_w$, for both the low- and high-speed regions. These values were determined from the velocity profiles in their corresponding regions in figure 5. Shown for comparison are the wall-shear curves for the Blasius flow and for the turbulent flat-plate boundary layer. The latter was determined from the empirical power-law relationship for the skin friction given in White (1974):

$$C_f \approx 0.026 Re_x^{-\frac{1}{7}},$$

where

$$C_f = \left(\frac{2\nu}{U_\infty^2}\right)\left(\frac{\partial U}{\partial y}\right)_w.$$

Initially the Görtler-flow wall shear follows the Blasius curve closely. This changes dramatically by $x = 60$ cm where the shear in the high-speed region increases steadily until reaching a peak value at $x = 105$ cm that is roughly four times the Blasius value for that position. Correspondingly, the wall shear in the low-speed region decreases faster than the Blasius curve, but by $x = 80$ cm it too begins to increase with downstream distance and ultimately rises to almost three times the Blasius value. Further downstream, for $x > 100$ cm, the wall shear in the low- and high-speed regions

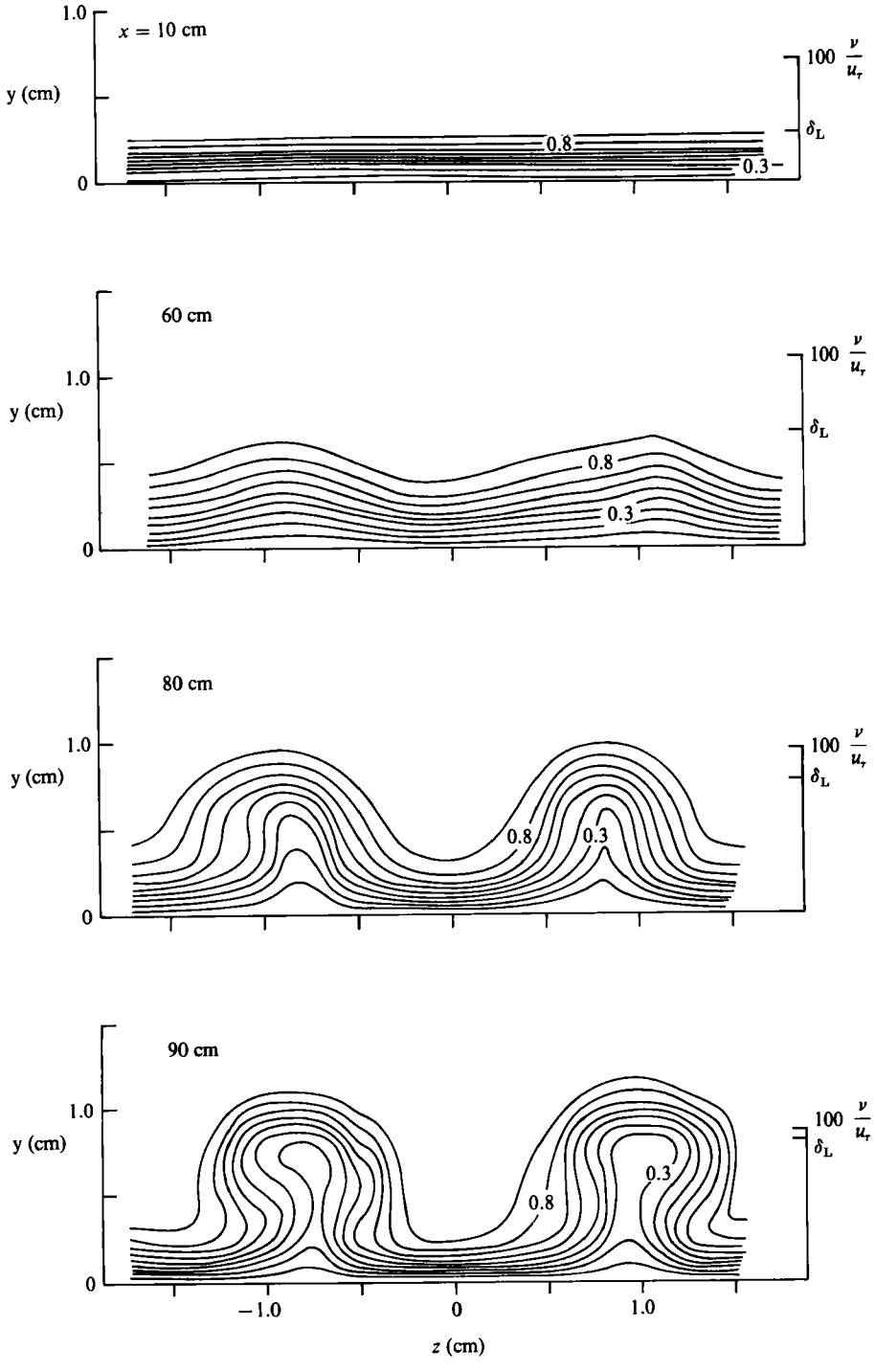

FIGURE 11. For caption see facing page.

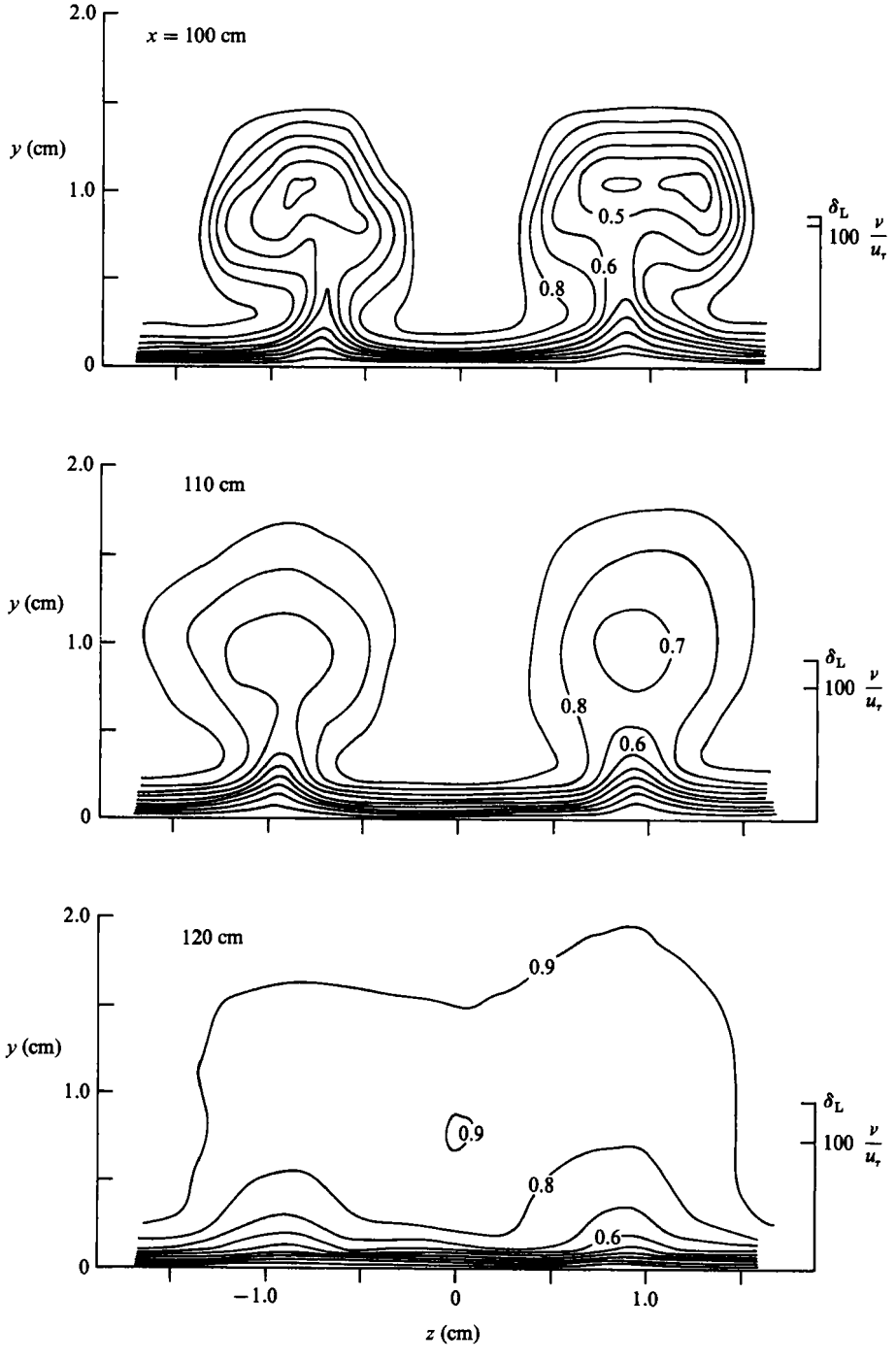

FIGURE 11. Iso-contours of the mean streamwise velocity in the cross-stream (y, z)-plane for various x. Nine contours are plotted with velocities of $U/U_\infty = 0.1, 0.2, \ldots, 0.9$.

equilibrates towards the same value indicating the return of homogeneity in the spanwise direction. Again the explanation for this appears to be increased mixing brought about as the flow transitions to turbulence. Note that the measured wall shear does not follow the turbulent-boundary-layer curve at the downstream locations even though observation of the temporal velocity signals indicates that the flow is essentially turbulent. This is probably because the turbulent boundary layer is not fully developed at these locations.

Subsequent plots will use the wall parameters for non-dimensionalization; i.e. the friction velocity u_τ and the kinematic viscosity ν. For this purpose a unique wall-shear curve was defined by calculating a spanwise-averaged $U(y)$-velocity profile from which the shear at the wall was found. The dotted curve in figure 10 represents a third-order least-squares fit of these data. It will be used for non-dimensionalization of data taken downstream of $x = 60$ cm; the Blasius values will be used at locations upstream.

4.4. *Growth of the vortex system*

To investigate the detailed structure of the developing low-speed regions, streamwise velocity measurements were made using the y-rake described previously at 33 spanwise locations covering two low-speed streaks. This technique produced a grid of 330 streamwise velocity measurements in the (y, z)-plane. The mean and r.m.s. velocities were calculated and stored. This process was repeated at a number of streamwise locations. Iso-velocity contours were then generated from the raw (y, z)-plane data grid by using a tensioned-spline fit to determine a velocity profile at each of the spanwise measurement locations. Velocities were then calculated at 100 uniformly spaced points in y for each of the profiles and a grid search was performed to obtain iso-velocity contours in $0.1U_\infty$ increments. Figure 11 shows iso-velocity contours of the mean streamwise velocity component for a number of downstream locations. The contour plots have the same lengthscales in the normal and spanwise coordinate directions and the spanwise origin has been chosen between the two low-speed streaks pointed out with the arrows in figure 4. The corresponding Blasius boundary-layer thickness δ_L and the viscous lengthscale ν/u_τ are given on the ordinate for each streamwise location. The friction velocity was determined from the average-wall-shear curves of figure 10.

Initially the boundary layer appears to be unperturbed in the spanwise direction (i.e. initially the boundary layer is Blasius-like). This situation quickly changes and by $x = 40$ cm downstream the action of the counter-rotating streamwise vortices has become evident. Low-momentum fluid lying between two vortices has been moved away from the wall at $z \approx \pm 1.0$ cm. This action promotes a thicker boundary layer which appears as a low-speed region when viewed at a constant elevation above the wall. Since the mean flow field was steady in time, the low-speed regions could always be identified with distinct smoke-filled streaks as in the photograph of figure 4.

Further downstream, the effects of the streamwise vorticity have become very pronounced, as seen at $x = 100$ cm. The low-speed streaks have grown in the normal direction much faster than the corresponding Blasius boundary layer and extend out to approximately $2\delta_L$. Most interesting, however, is the fact that $U(y)$ is no longer single-valued. Low-momentum fluid is found riding above higher-speed fluid producing highly unstable S-shaped velocity profiles in the normal direction as will be seen later. Regions of intense shear, identified by the small distance between iso-velocity lines, are also found on the sides of the low-speed streaks producing inflexional profiles in the spanwise direction as well. These unstable profiles appear

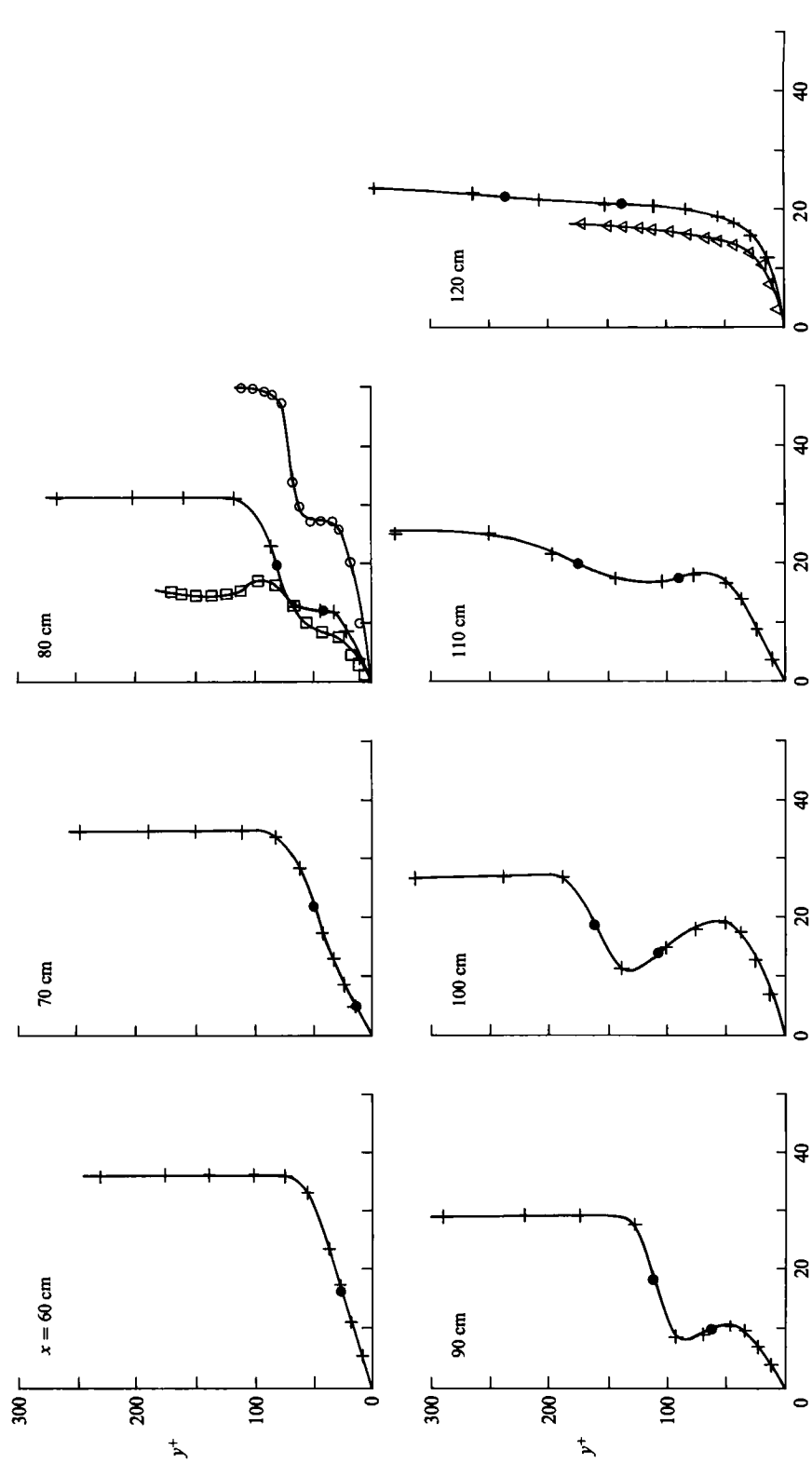

FIGURE 12. Inflexional normal profiles of the mean streamwise velocity taken at the centre of a single low-speed region for various x. At $x = 80$ cm, comparison is made with the transitional flat plate (Kovasnay *et al.* 1962) (○) and the turbulent-boundary-layer ejection (Grass 1971) (□). At $x = 120$ cm, comparison is with the mean turbulent-boundary-layer profile of Grass (△). +, Present study; ●, inflexion point.

in the same regions where the oscillations are apparent in the flow-visualization photographs. Exactly the same behaviour was observed by F. X. Wortmann & M. Strunz (1975, unpublished report, Institut für Aerodynamik und Gasdynamik, Universität Stuttgart). Downstream of the $x = 100$ cm position the spanwise structure collapses very quickly. As in the equilibration of displacement thickness across the span in figure 9, the flow visualizations suggest that this results from increased mixing owing to the onset of turbulence.

Streamwise vortices initiated by the Görtler instability exist in a strong mean gradient of streamwise velocity $U(y)$. Thus, between two vortices in the spanwise direction the induced motion acts to remove low-momentum fluid away from the wall, as seen near $z = \pm 1.0$ cm. One half-wavelength away, the vortices pump high-speed fluid towards the wall. The low-speed regions that result from this lift-up of low-momentum fluid eventually develop to the extent that the velocity profiles are inflexional, as illustrated in figure 12. The profiles presented were taken at the centre of a low-speed region and are plotted in terms of wall units u_τ and ν. Examples of inflexional profiles for both the transitional and fully turbulent flat-plate boundary layers are also given for comparison with the profile at $x = 80$ cm ($G\ddot{o}_\theta = 6.15, Re_\theta = 343$). The instantaneous transitional flat-plate profile was obtained from Kovasnay, Komoda & Vasudeva (1962) and has $Re_\theta \approx 540$. The turbulent-boundary-layer profile is from the smooth boundary data of Grass (1971) for an ejection at $Re_\theta \approx 280$.

Of note in the sequence of profiles is the evolution of the inflexion-point development. Inflexion points, plotted as solid circles, for the Görtler-flow profiles were determined by carefully fitting a smoothing cubic-spline approximation to the data and finding the zeros of its second derivative. Care was taken to ensure that the data fit was sufficiently smooth so as not to produce erroneous inflexion points. A single point of inflexion first appears in the region $20 < y^+ < 30$; i.e. in a region adequately removed from the wall so that the effects of viscosity are relatively unimportant. As the velocity defect in this region grows the profiles evolve to an S-shaped state with two points of inflexion, as seen at $x = 80$ cm. The comparable transitional and turbulent flat-plate instantaneous profiles are of similar shape and in all three cases the points of inflexion fall in the region $30 < y^+ < 70$. Also of interest is the fact that the velocity gradients at the points of inflexion have the same order of magnitude as the wall gradient. Proceeding downstream, the points of inflexion move progressively further from the wall (in wall units *and* in physical units) and the velocity defect increases with a consequent steepening of the velocity gradients to the point where they actually exceed the wall gradient. Downstream of $x = 100$ cm, the velocity-defect region rapidly decreases and ultimately achieves a standard-looking turbulent-boundary-layer profile with no points of inflexion. Shown for comparison at the 120 cm location is the mean turbulent smooth-wall velocity profile of Grass.

Figure 13 shows the downstream development of the inflexional spanwise profiles of streamwise velocity. The profiles were not obtained at the same y-location but at the y-position corresponding to the highest spanwise shear as seen in figure 11. The profiles are normalized with U_∞ (instead of the wall units) and the solid circles represent inflexion points determined by the method described for the $U(y)$-profiles. As mentioned earlier, the spanwise variation in velocity is caused by the presence of streamwise vortices and their induced motion which lifts low-momentum fluid away from the wall in a spanwise periodic fashion. As a result of this, inflexional-type spanwise profiles evolve early in the flow development. The basic notion of instability through a system of streamwise vortices of altering rotational sign implies that $U(z)$

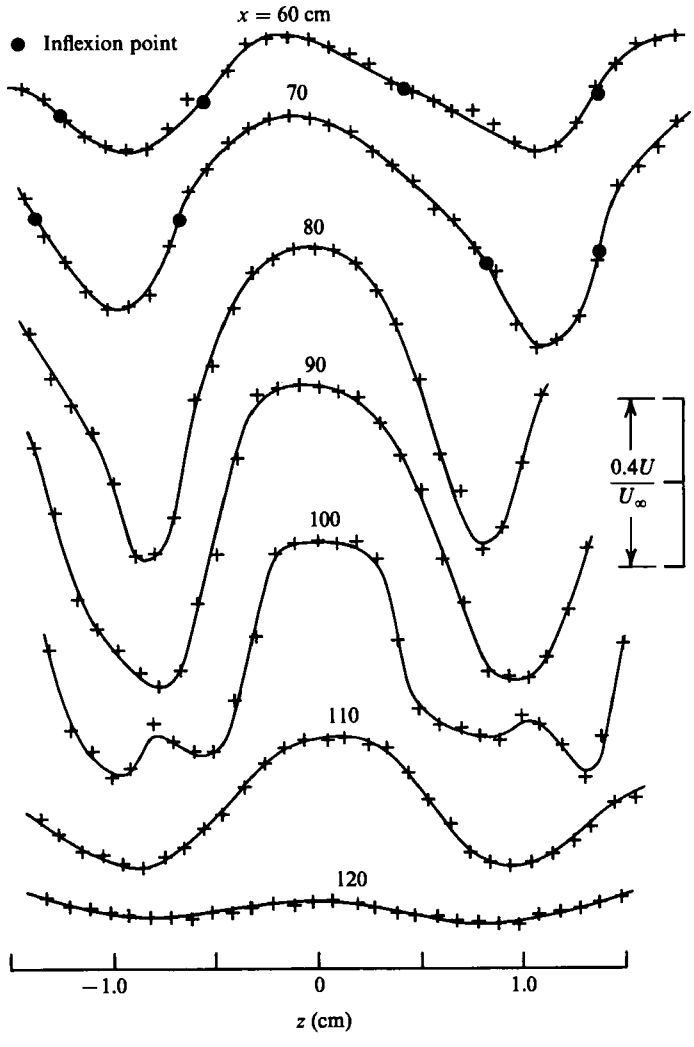

FIGURE 13. Inflexional spanwise profiles of the mean streamwise velocity for various x taken at the y-position of highest spanwise shear.

is inflexional at the onset of instability (i.e. typically at $G\ddot{o}_\theta > 0.3$ which corresponds to $x \approx 1.5$ cm for the prevailing flow conditions). In comparison, unstable $U(y)$-type profiles do not manifest themselves until 60–70 cm downstream, as seen in figure 12.

A point of note is the similarity between the spanwise profiles of figure 13 and a typical unstable plane-wake profile (see for example Sato & Kuriki 1961). As in the case of a plane wake, the spanwise Görtler flow profiles for various downstream locations become nearly similar in shape when normalized with a local velocity and width. This feature suggests that developing instabilities associated with the low-speed region might behave similarly to those in the plane wake. Mattingly & Criminale (1972) have shown that the most unstable disturbances in the wake produce transverse oscillations of the mean profile corresponding to a sinuous disturbance mode. This mode dominates the less-amplified varicose disturbance mode everywhere in the near-wake region.

(a)

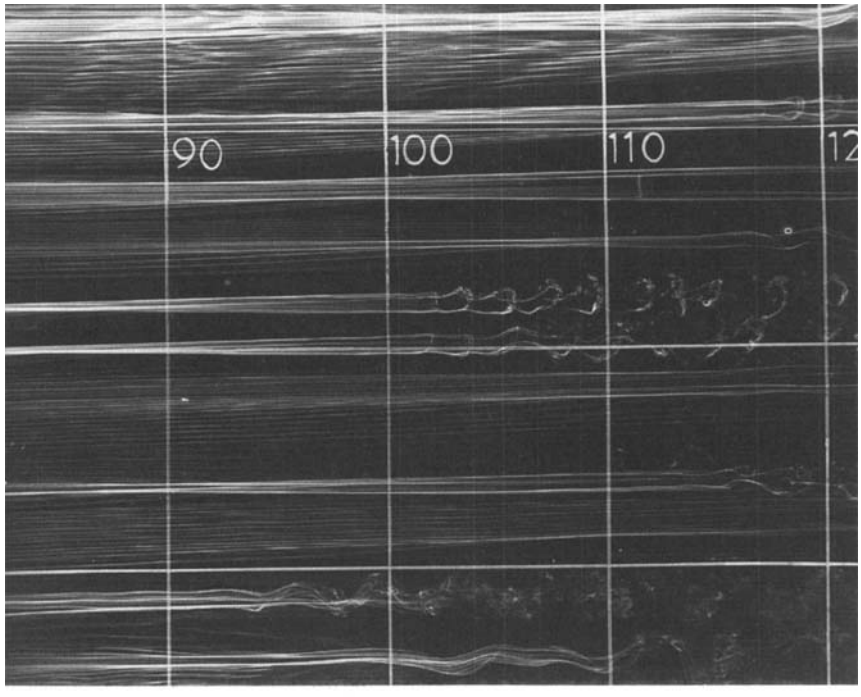

(b)

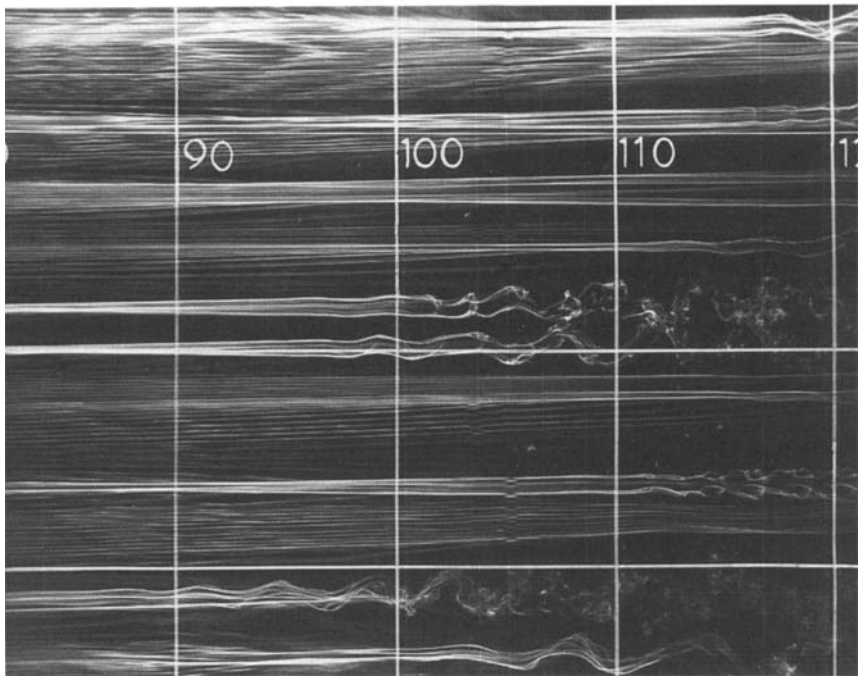

FIGURE 14(a,b). For caption see facing page.

(*c*)

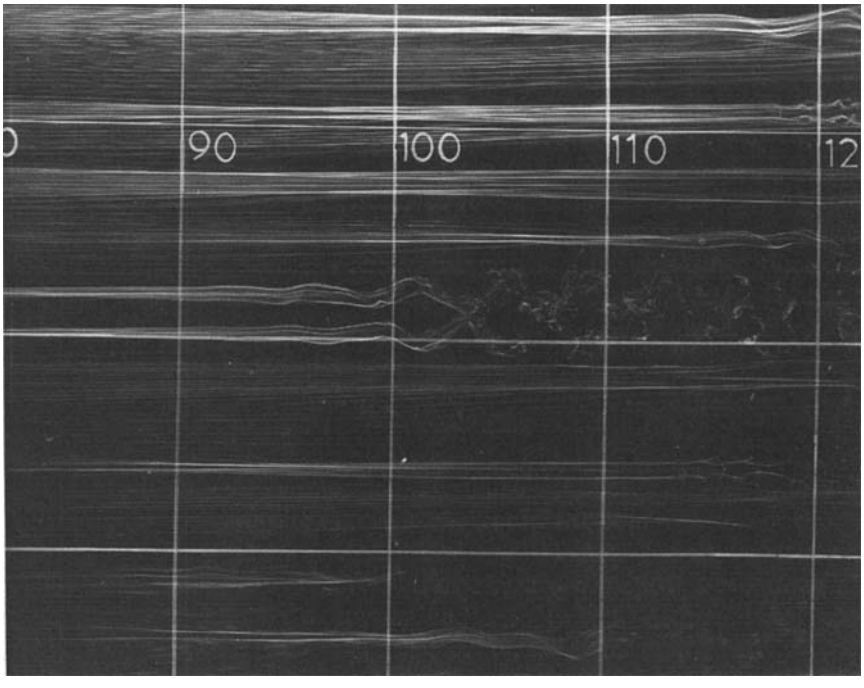

FIGURE 14. Instantaneous visualizations showing secondary instability modes: (*a*) horseshoe vortex mode, (*b*) combined horseshoe vortex and sinuous modes, (*c*) sinuous mode. The smoke wire is located at $x = 54$ cm and $y/\delta_L = 0.3$.

4.5. *Laminar–turbulent transition*

The primary aim of this study is to understand the dynamics of the vortices and how they transition to turbulence. It is evident from the photographs of figure 14 that the low-speed streaks developed by the vortex field experience periodic oscillations prior to transition. Two different modes of secondary instability were observed to proceed the breakdown of the low-speed streaks. Streaklines of the type seen in the middle of figure 14(*a*), i.e. $100 < x < 110$ cm, have often been used to suggest that a horseshoe vortex structure is involved in the events during which most of the turbulence production occurs. This mode of instability has been observed in several other Görtler flow studies including those by Jeans & Johnston (1983), Aihara & Sonoda (1981), and Aihara & Koyama (1981). It is suggested that the shear layer formed on the interface between the low-speed streaks and the outer high-speed flow rolls up as the result of a Helmholtz-type instability. From the sequence of realizations shown in figure 14 it is also evident that the horseshoe vortex street appears at irregular intervals periodically being replaced by a second mode of instability. The sinuous transverse oscillation of the streaklines in the middle of figure 14(*c*) is an example of this second mode of instability. The occurrence of a sinuous oscillation mode for the Görtler flow transition has also been reported by Bippes (1972). This type of motion is also familiar in unsteady Couette flow as reported by Coles (1965) and for the streaks observed in fully turbulent flat-plate boundary layers (see for example Kline *et al.* 1967 and Kim *et al.* 1971). Although two modes of instability were observed here, the sinuous oscillation mode was the

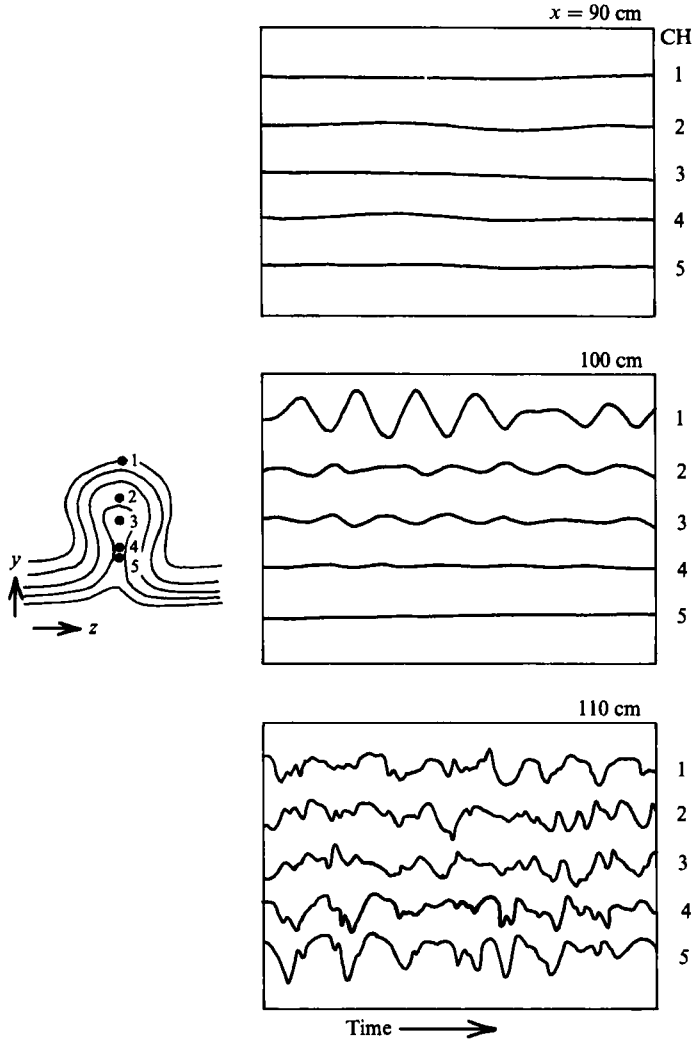

FIGURE 15. Time traces of simultaneous streamwise velocity fluctuations at five y locations as indicated and for various streamwise positions. The spanwise location corresponds to the centre of a single low-speed region.

one most often found and it appears to be the one most consistent with the velocity data. This same two-mode behaviour was also noted by Jeans & Johnston.

It should be noted here that the visualization technique employed is subject to a history effect that makes interpretation of localized behaviour such as this difficult and opens the possibility that the smoke pattern may not be an effective representation of the local flow field (see for example Smith 1984). However, based on visualizations made with the smoke wire at other locations in x and y, the two-mode behaviour observed is reproducible independent of the location of tracer introduction.

Evidence presented thus far suggests that the regular oscillations of the low-speed streaks seen in figure 14 result from a localized free-shear-layer-type instability on the unstable velocity profiles as shown in figures 12 and 13. Examples of the natural fluctuations associated with the breakdown of the low-speed streaks are shown in the

oscillograms of figure 15 for several downstream locations. The traces are from five hot-wire sensors at different y-locations and at the spanwise position corresponding to the centreline of a single low-speed region. As seen at $x = 90$ cm, very few fluctuations were observed for $x < 100$ cm. Nearer $x = 100$ cm, a well-defined oscillation of approximately 130 Hz becomes evident in the outer portion of the boundary layer. This occurs at approximately the same streamwise location as where the regular sinuous motion of the streaks becomes visible in figure 14. The observed natural frequency here compares well with the most amplified disturbance predicted by the spatially growing shear-layer-stability theory of Michalke (1965). Based on the local shear-layer thickness and the velocity difference ascertained from figure 11 at $x = 100$ cm the predicted natural frequency is approximately 157 Hz. Downstream of the $x = 100$ cm position, the fluctuations rapidly become random indicating breakdown to turbulence as manifested by the velocity traces for $x = 110$ cm.

Figure 16 shows the distribution of the temporal velocity fluctuations in the (y, z)-plane for a number of downstream locations by plotting contours of constant $u'_{\rm rms}$. These data were obtained in a similar manner to the iso-mean velocity contours presented in figure 11 and are shown with the same y- and z-scaling as in the earlier figure. The contours are plotted in increments of $0.01\,U_\infty$. Comparing this figure with figure 11 shows that the developing fluctuations are associated with the low-speed streaks. Note the presence of two peaks in the $u'_{\rm rms}$ distribution and that they are located on the sides of the low-speed regions. This observation was not coincidental; the two-peak distribution was found at all streamwise locations in the developing flow field. This result led to one of the principal conclusions of this research; namely the vortices are susceptible to a secondary instability which is governed by the inflexional velocity profiles in the spanwise direction as discussed below.

As breakdown is approached, a secondary peak in the $u'_{\rm rms}$ distribution develops near the wall, typically for $x \geqslant 90$ cm. It has a smaller scale but ultimately attains the highest amplitude in the evolution of the streamwise vortices. This occurs downstream of the point where the flow has already broken down into a turbulent state. Note that for the $x = 120$ cm location, the contours very near the wall have been omitted owing to lack of adequate probe resolution in this region.

As evidenced by the $U(z)$-profiles previously shown, the boundary layer is unstable to streamwise vortices that grow in the downstream direction. Bippes (1972) observed that the growth rate of these vortices is relatively small and that a secondary instability ultimately produces the fluctuations that lead to turbulence. Thus the vortices themselves do not directly breakdown to turbulence, but set up a flow field that is unstable to other instabilities with high growth rates. The growth of both the streamwise vortices and the developing temporal velocity fluctuations associated with transition to turbulence are shown in figure 17. A direct measure of the growth of the vortices was not possible so a representative measure of their growth was determined from the spanwise variation of the mean streamwise velocity caused as the laminar flow field is deformed by the presence of the streamwise vortices. Plotted in figure 17 are the maximum r.m.s. amplitudes of this spanwise variation for each downstream location. The growth of the spatially averaged r.m.s., presumably a measure of the growth of the vortices, is essentially exponential until 70–80 cm downstream. The spanwise variation reaches a maximum at around $x = 90$ cm and thereafter declines rapidly indicating a homogenization of the flow. Also plotted in figure 17 for each x-location are the maximum temporal fluctuation levels corresponding to one of the peaks in the $u'_{\rm rms}$ distributions of figure 16 (it was irrelevant which of the two peaks was chosen). The temporal velocity fluctuations develop

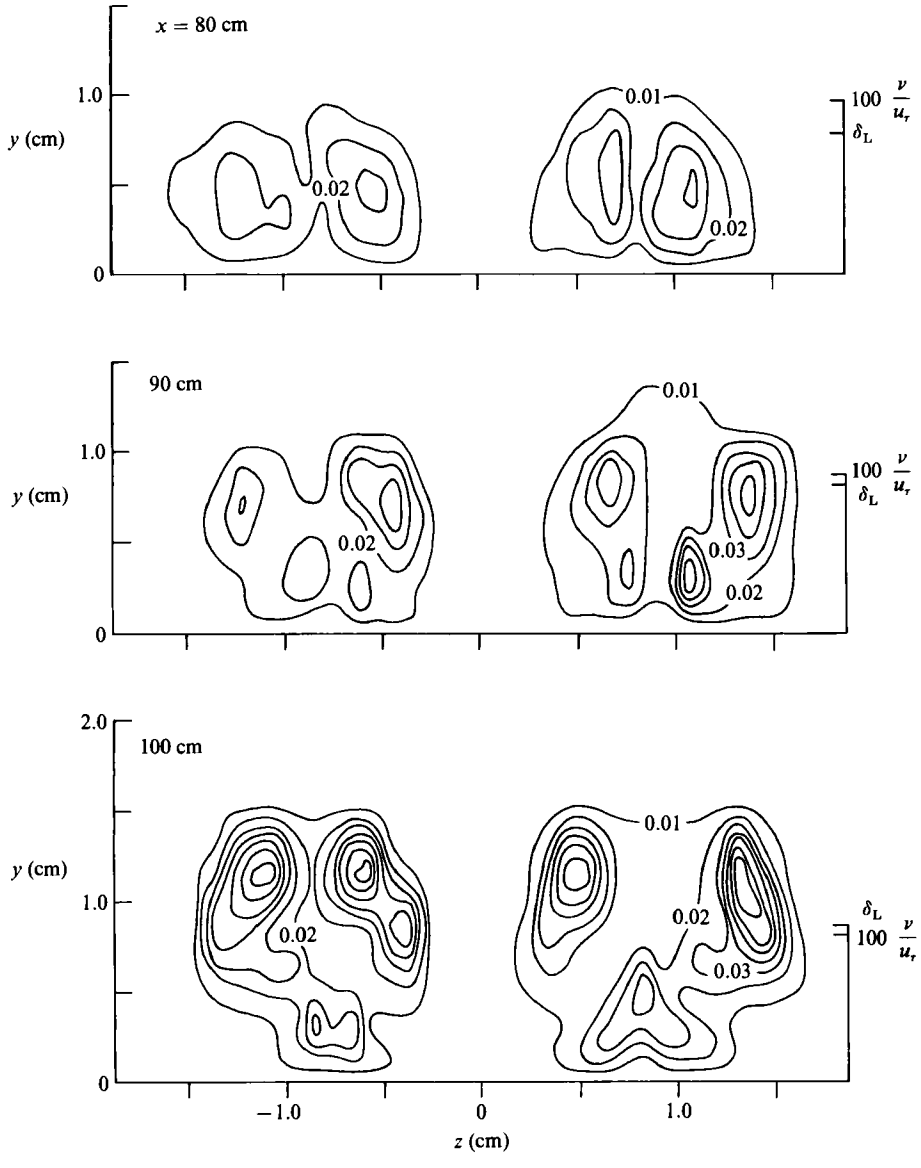

exponentially until $x = 100$ cm. Ultimately the amplitude of the fluctuations saturates as seen in the oscillograms of figure 15 for $x = 110$ cm. This figure clearly shows the effect of the developing fluctuations on the spanwise structure created by the original Görtler instability: the rapid increase in temporal fluctuations occurs in the region where the spanwise structure begins to be smeared out as seen for the $x = 100$–120 cm locations in figure 11. This is explained by the increased mixing associated with the onset of turbulent fluctuations.

Of note in figure 17 is the comparison between the growth rates of the two instabilities, i.e. the original Görtler instability and the instability associated with the inflexional profiles that produce the temporal velocity fluctuations. In the

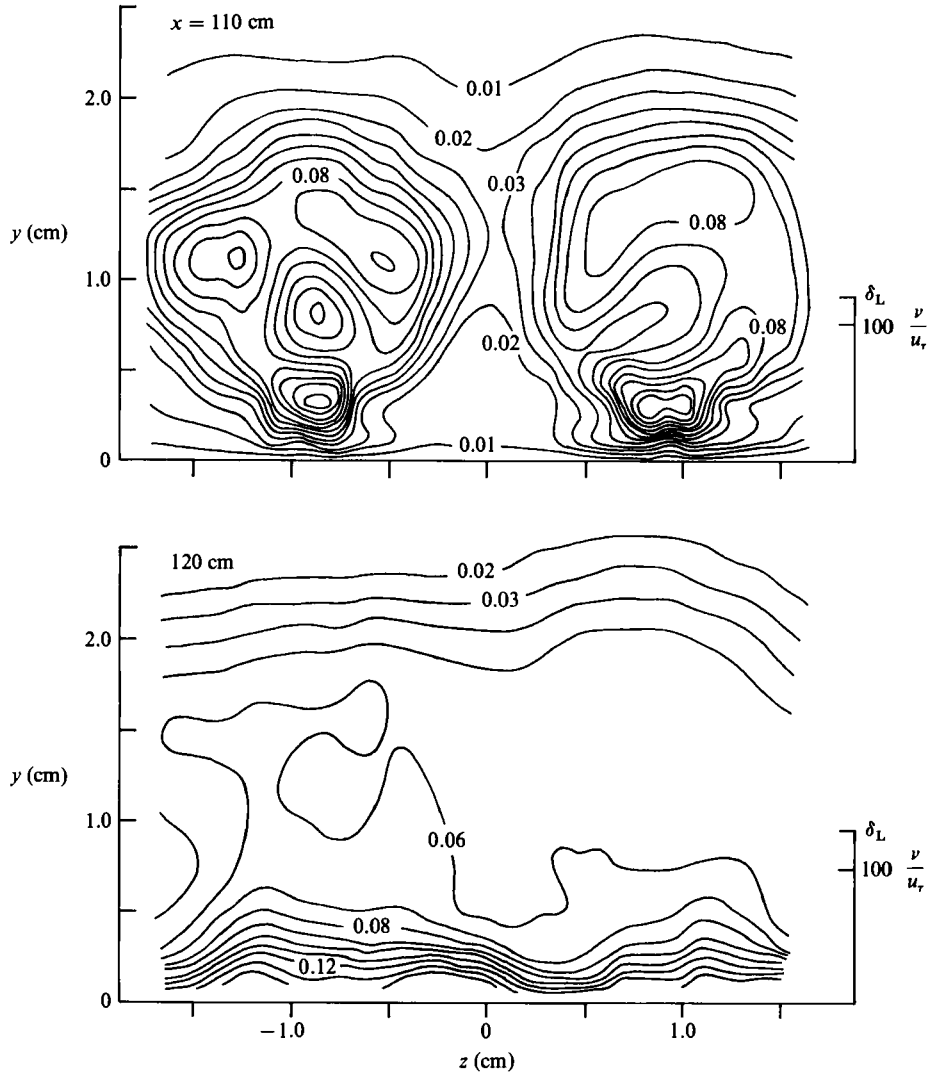

FIGURE 16. Iso-contours of the streamwise velocity fluctuations in the cross-stream (y, z)-plane. Contours are plotted with fluctuation levels of $u'_{\rm rms}/U_\infty = 0.01, 0.02, \ldots$.

spatially developing stability analyses of the Görtler flow (i.e. Smith 1955; Floryan & Saric 1982), the disturbance field is assumed in the form $F(y)\,e^{\beta x}\cos kz$, where β is the streamwise growth rate ($\beta > 0$ indicates amplified disturbances). Given the uncertainty in the estimates for these growth rates, the important feature is *not* in their absolute magnitudes but rather in the relative comparison between the two. The conclusion, thus, is that the growth of the secondary instability exceeds the growth of the initial instability that produced the streamwise vortices by a factor of approximately two to five. This result is in agreement with the findings of Bippes stated earlier. Additionally, the growth rates estimated for the vortex field compare favourably with the theoretical predictions.

To investigate the nature of the two-peaked $u'_{\rm rms}$ distribution in figure 16 discussed previously, the shear associated with the inflexional velocity profiles in y and z was

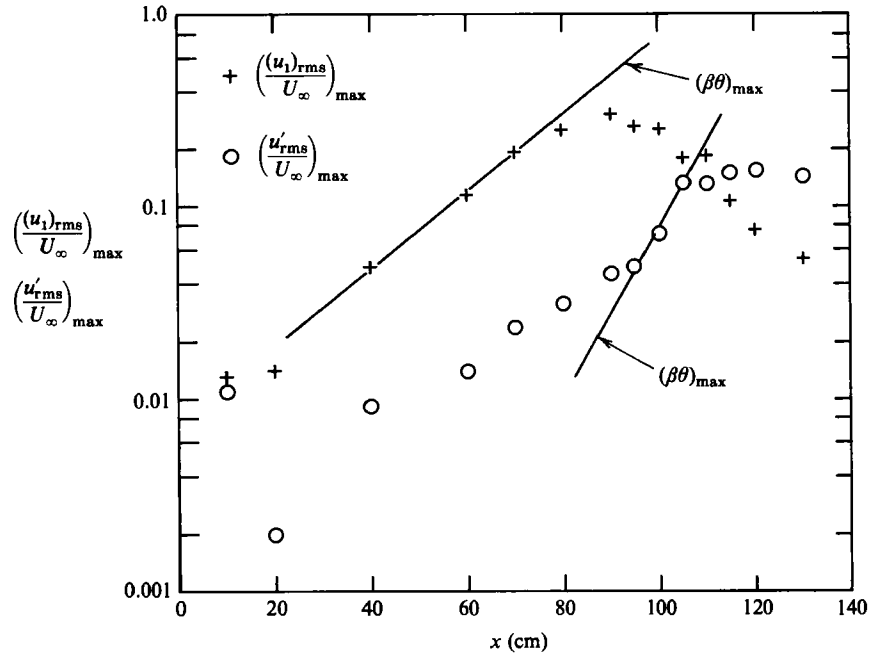

FIGURE 17. Comparison between the streamwise growth of the temporal velocity fluctuations, $(u'_{rms})_{max}$, and the growth of the streamwise vortical disturbance, $(u_1)_{max}$.

explored. Since the raw data used to obtain figure 11 had been fitted with a spline and calculated for a fine mesh grid, its derivatives could also be calculated in the (y, z)-plane and thus iso-shear contours determined. Figure 18 (a, b) shows the $\partial U/\partial y$ and $\partial U/\partial z$ iso-shear contours respectively for the $x = 100$ cm location. The contours are plotted in increments of $0.25(\partial U/\partial y)_w$, where $(\partial U/\partial y)_w$ is the average gradient at the wall as determined previously in figure 10. In both plots regions of negative shear are shown with dashed-line contours. In figure 18 (a), strong positive $\partial U/\partial y$ shear is found near the wall with the peak in the high-speed region between the low-speed streaks. This high-shear region is indicative of the thinner boundary layer there. Under the low-speed streak, where the boundary layer is thicker, the shear is smaller. In addition to the strong shear at the wall, there are regions of strong positive and negative shear removed from the wall in the vicinity of the low-speed streaks of figure 11. These occur at locations near the positions of inflexion in the $U(y)$-profiles presented previously and are the same order of magnitude as the shear at the wall. The distribution of $\partial U/\partial y$ shear in the (y, z)-plane can be compared with the u'_{rms} distribution and it is observed that the locations of the maxima in the fluctuations do *not* occur in the same regions as where peaks are found in the shear contours, as would be expected if the $U(y)$-instability were the cause of the oscillations.

Figure 18 (b) gives the corresponding contours of $\partial U/\partial z$ shear. As in figure 18 (a) the regions of high shear are located in the vicinity of the low-speed streaks and are of the same order of magnitude as the $\partial U/\partial y$ shear at the wall. The peak-shear locations occur near the points of inflexion identified in the corresponding $U(z)$-profiles presented in figure 13. As with the preceding plot, the distribution of $\partial U/\partial z$ shear can be compared with the u'_{rms} distribution. The peaks of these two distributions correlate very well indeed, strongly suggesting that the developing oscillations are

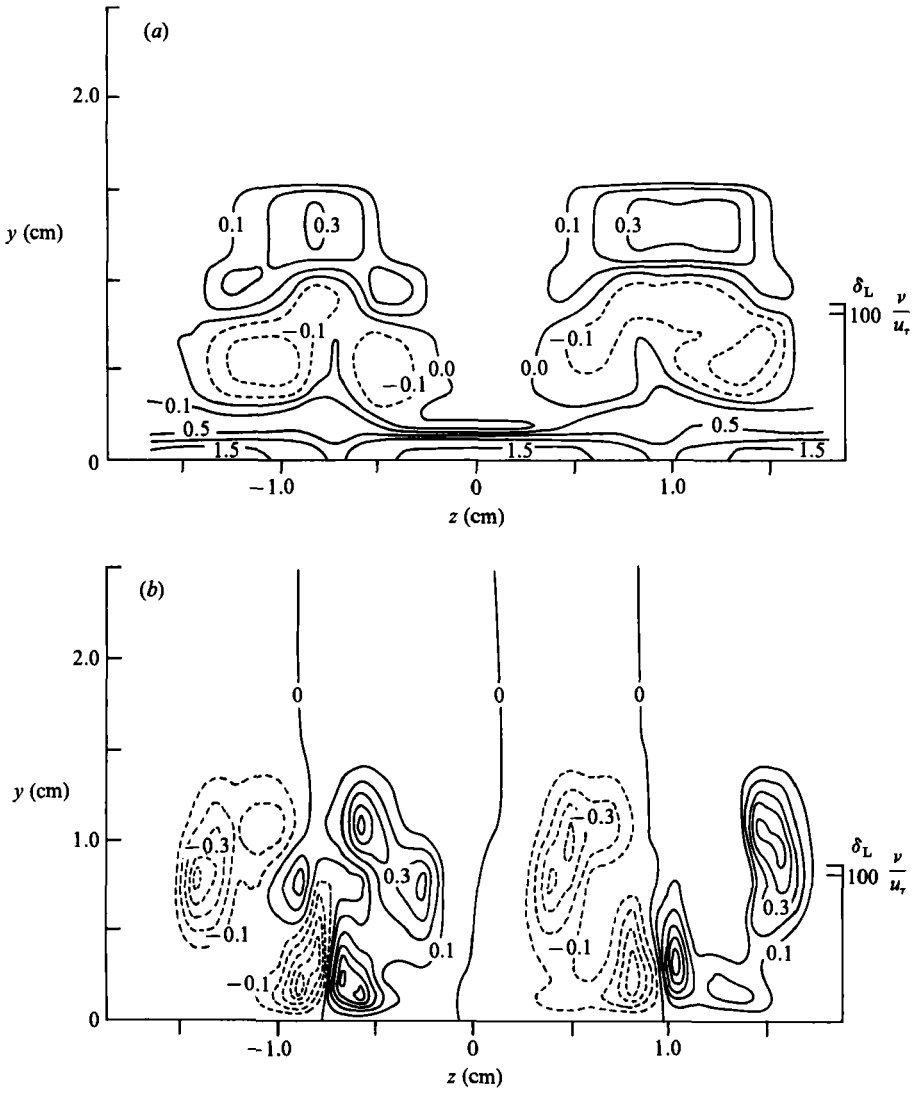

FIGURE 18. Iso-shear contours in the cross-stream (y, z)-plane for $x = 100$ cm. Contours are normalized with $(\partial U/\partial y)_w$ from figure 10: (*a*) $\partial U/\partial y$ shear contours; (*b*) $\partial U/\partial z$ shear contours.

the result of the unstable velocity profile in the spanwise direction, i.e. $U(z)$, and are not due to the inflexional $U(y)$-profile. Such an instability would produce a u- and w-velocity fluctuation instead of u and v, which is consistent with the oscillations observed in the photographs of figure 14. In addition, the $\partial U/\partial z$ shear has developed another strong peak nearer the wall; i.e. at $y^+ \approx 30$ which has the same strength as the primary $\partial U/\partial z$ peaks at $y > \delta_L$. This $\partial U/\partial z$ shear is responsible for the large u' region near the wall noted in figure 16. These measurements are in good agreement with Komoda's (1967) result that localized intense vertical shear layers develop on the sides of the low-speed regions and were responsible for the eventual breakdown of the streamwise vortices. The data of Nishioka & Asai (1984) also indicate that strong spanwise shear exists during the final stages of transition in channel flow.

4.6. *Effects of velocity perturbation*

A periodic acoustic disturbance was introduced into the flow at the wall through a 0.5 mm diameter orifice located 60 cm downstream of the plate leading edge; the spanwise location corresponded to the low-speed streak pointed out by the arrow in the visualization of figure 4 at approximately 8.0 cm below the test-plate centreline. The flow fluctuations downstream of the perturbation were observed using a spanwise rake of 12 hot-wire sensors spanning one or more low-speed streaks. The forcing signal was used as a phase reference for conditionally sampled measurements. In all cases, the forcing amplitude was adjusted so that it was just large enough to effectively lock the fluctuations to the forcing signal. Typically, the amplitude of the velocity fluctuation, $(u'_{\rm rms})_{\rm max}/U_\infty$ with and without the forcing was 0.07 and 0.08 respectively, a difference of roughly 15 %. Distributions of $u'_{\rm rms}$ in the (y, z)-plane of the type seen in figure 16 measured with and without forcing show virtually no qualitative difference.

Figure 19 shows simultaneous hot-wire time traces at a number of z-positions for various forcing frequencies but at fixed amplitude. The hot-wire rake was positioned at $x = 95$ cm and $y = 0.8$ cm where the maximum fluctuation amplitude was observed in the $u'_{\rm rms}$ distributions of figure 16. The flow fluctuations can be effectively locked to the forcing signal over a range of approximately 70 Hz $< f_{\rm forcing} <$ 200 Hz for $U_\infty = 500$ cm/s. Below a forcing frequency of 70 Hz the flow fluctuations can be locked to the forcing frequency but the response is at a harmonic (typically the first harmonic) of the forcing. This is demonstrated in figure 19 (*a*) for $f_{\rm forcing} = 60$ Hz. The response for a forcing frequency of 70 Hz shows a mixed behaviour, i.e. the response can have both fundamental and harmonic content as seen in figure 19 (*b*, *c*). Above 70 Hz, the oscillations appear to strictly be a fundamental response as in figure 19 (*d*).

Of note in the oscillograms is that the fluctuations are 180° out of phase across the span of a single low-speed streak. This observation is consistent with the sinuous oscillation observed to precede breakdown in the flow-visualization photographs. This type of behaviour is also consistent with the primary mode of instability for a two-dimensional wake (see for example Sato & Kuriki 1961) and the fact that the fluctuations develop as the result of an unstable 'wake-like' profile in z as in figure 13.

The primary reason for introducing artificial perturbations into the flow was to produce a phase reference so that the eddy structure associated with the breakdown of the low-speed region could be educed through the use of phase averaging. Figure 20 (*a*) shows individual realizations of the phase-averaged spanwise profile of streamwise velocity $\langle u(z) \rangle$ over one cycle of the perturbation. The y-location corresponds to the peaks in the $u'_{\rm rms}$ distribution previously shown for $x = 100$ cm. The forcing was at the observed natural oscillation frequency of 130 Hz and the phase average was taken over roughly 1000 cycles of this perturbation. In these plots, time increases to the left to simulate a rightward-travelling flow. The sinuous lateral motion observed in the smoke-wire visualizations of figure 14 (*b*, *c*) was very obviously present for this particular y-location. This sinuous motion was present, in fact, for all y-locations across the low-speed streak, lending support to the idea that the ultimate mode of breakdown occurs through instability of the spanwise profile $U(z)$.

In figure 20 (*b*), iso-contour plots of the phase-averaged streamwise velocity component in the (z, t)-plane again show evidence of the sinuous lateral motion. Also evident are localized regions of high shear as the motion reaches its extrema in the spanwise direction (i.e. regions of small Δz between lines). The spanwise locations of these localized high-shear regions correspond as expected to the two peaks in the $u'_{\rm rms}$

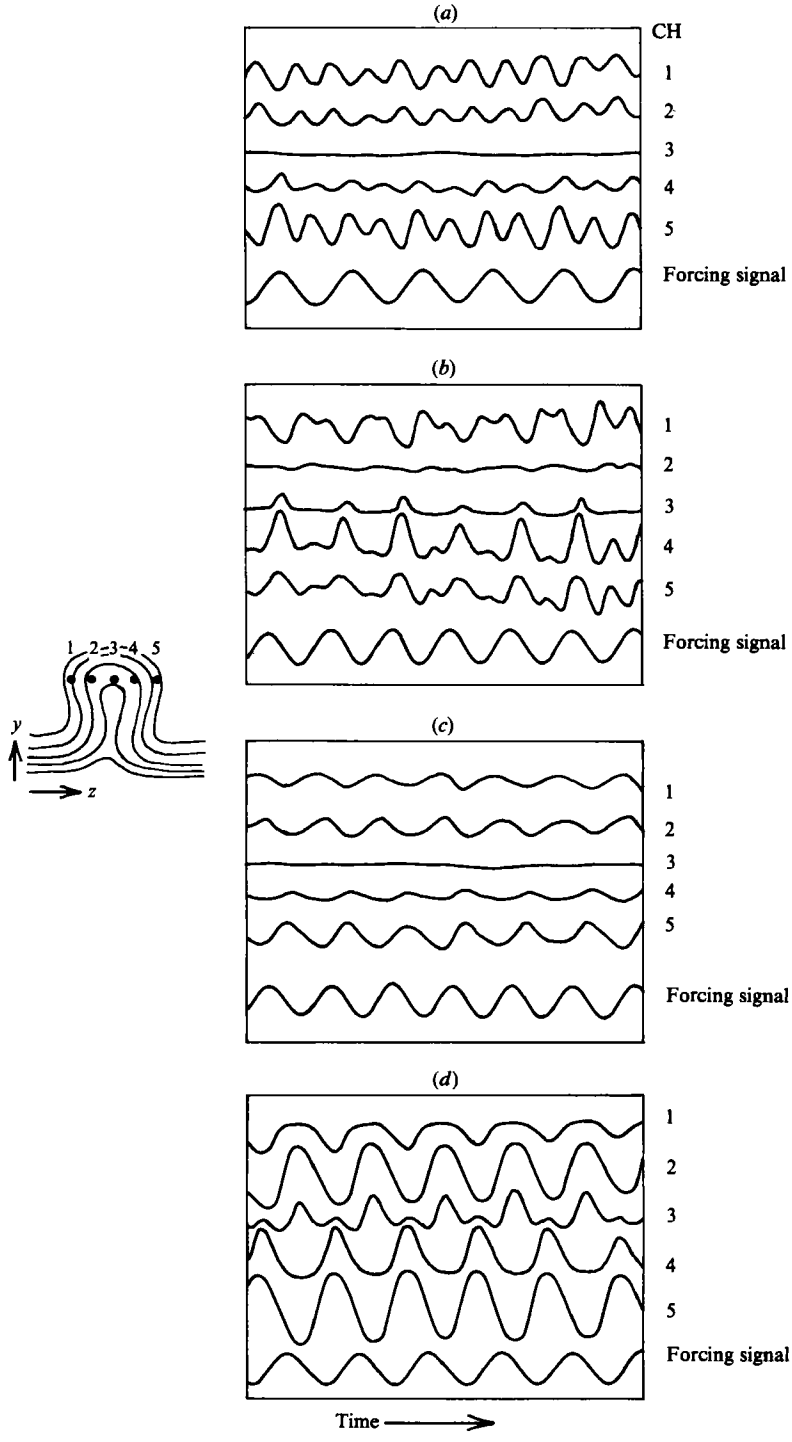

FIGURE 19. Time traces of simultaneous streamwise velocity fluctuations at five z-locations as indicated and for various forcing frequencies (*a*) 60 Hz, (*b*, *c*) 70 Hz, (*d*) 120 Hz. The y-location corresponds to the peak in the u'_{rms} distribution as in figure 16 but for $x = 95$ cm.

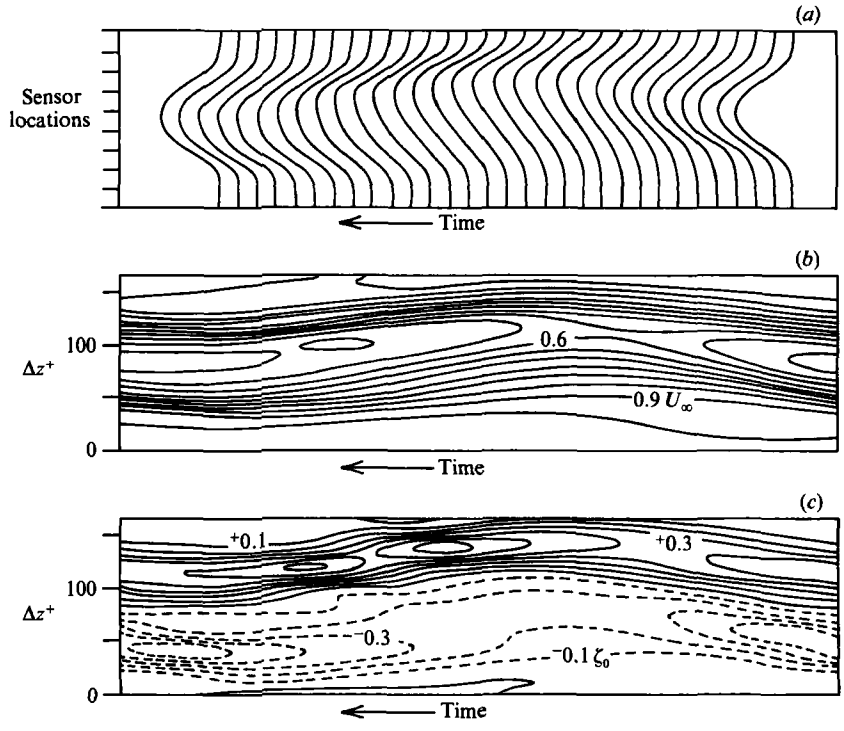

FIGURE 20. (*a*) Phase-averaged spanwise profiles of the streamwise velocity $\langle u(z)\rangle$ at $x = 100$ cm. (*b*) Iso-contours of the phase-averaged streamwise component of velocity in the (z,t)-plane. Contours are plotted in increments of $\langle u\rangle/U_\infty = 0.1$. (*c*) Iso-shear contours of $\partial\langle u\rangle/\partial z$ in the (z,t)-plane. Contours are normalized with the average wall gradient $\zeta_0 = (\partial U/\partial y)_w$.

distributions shown in figure 16. These regions of high shear can be seen clearly by plotting iso-shear contours in the (z,t)-plane, as done in figure 20(*c*). These were obtained in a manner similar to those of figure 18 by taking the z-spatial derivative of the spline fits to the profiles in figure 20(*a*). The negative-shear lines are again shown as the dashed curves. Iso-shear plots for other y-positions display qualitative similarity to the one presented in figure 20(*c*) except that the relative position of the high-shear regions during the oscillation cycle changes as distance from the wall is increased. This suggests that the localized high-shear regions (in time and z) are inclined at some oblique angle to the wall. This value was determined to be approximately 17° by following the movement of these localized regions through the boundary layer and utilizing a propagation velocity of $0.8U_\infty$, estimated from the outer inflexion point in figure 12 at $x = 100$ cm. This inclination of the eddy structure associated with breakdown compares favourably with that given for a turbulent flat-plate boundary layer (see for example Brown & Thomas 1977).

5. Conclusions

The growth and breakdown of counter-rotating streamwise vortices, generated on a concave wall via the Görtler instability mechanism, were experimentally studied as a model for comparable eddy structures that exist in transitional and turbulent

flat-plate boundary layers. The naturally occurring vortices were examined using the smoke-wire visualization technique and multiple-probe hot-wire rakes.

Results derived from this study show that the initially Blasius boundary layer on the concave wall rapidly becomes three-dimensional as a system of streamwise vortices is established in accordance with the linearized stability analysis of Görtler. Downstream, the vortices grow and the flow field ultimately breaks down and transitions to turbulence near $G\ddot{o}_\theta \approx 9$ as reported earlier by Liepmann (1945). The eddy lengthscales associated with the vortices (i.e. spanwise wavelength, streamwise extent, and streamwise wavelength of the secondary instability oscillations) compare favourably with those for both transitional and turbulent flat-plate boundary layers when scaled with the viscous parameters, ν and u_τ, as suggested by Blackwelder (1983).

The dynamics of the eddies found in these flow fields are also similar. The streamwise vortices exist in a strong mean gradient of streamwise velocity so that their motion induces low-momentum fluid away from the wall, forming elongated streaks of low-speed fluid lying between the vortices. The streaks are separated in the spanwise direction by regions of higher-momentum fluid induced towards the wall from the outer flow. The high-speed regions are of less importance in the developing flow because they have a more stable $U(y)$-profile. The low-speed streaks grow downstream faster than a nominally Blasius boundary layer and evolve to the state where lower-momentum fluid is found riding over higher-speed fluid, producing strongly inflexional streamwise velocity profiles in both the normal and spanwise directions. Instability oscillations develop on these unstable profiles that scale with the local shear-layer thickness and velocity difference. This secondary instability grows much faster than the original instability that produced the streamwise vortices and it rapidly leads to a chaotic breakdown and hence to turbulence. Thus, one of the conclusions from this study is that the streamwise vortices themselves do not transition directly but instead set up a localized inviscid shear-layer instability which eventually results in the turbulence. That is, transition takes place locally on each shear layer associated with an individual low-speed region until ultimately the entire flow field is turbulent. This is explained by the observation that the counter-rotating vortices that produce the low-speed regions were initiated by a random disturbance field so that each low-speed region has developed to a different state at any given point downstream in the flow field. Thus the local shear surrounding each low-speed region is slightly different. In this manner, each low-speed region transitions to turbulence at a different streamwise position determined by the local shear conditions. Far enough downstream, i.e. $G\ddot{o}_\theta \gtrsim 9$, all of the low-speed regions were turbulent and transition was complete; however a fully developed turbulent flow was only established further downstream.

One of the primary results from this research is that the secondary instability was associated more with inflexional velocity gradients in the spanwise direction than with the normal gradient of the streamwise velocity. This was most noticeable by comparing the measured fluctuation levels of figure 16 with the $\partial U/\partial z$ contours of figure 18(*b*). Contrary to expectations, the spatial scales of the r.m.s. fluctuations correlate better with $\partial U/\partial z$ than with $\partial U/\partial y$. In addition another eddy structure appears to develop near the wall at $y^+ \approx 30$. These fluctuations are also strongly correlated with a large $\partial U/\partial z$ shear at the same location and this structure ultimately develops the largest r.m.s. level. At this point, one could speculate that this developing structure results from a regeneration mechanism through induction of the

original vortices. However, further detailed study is required to establish this possibility.

The conclusions from this study should be compared to the existing models of both transitioning and fully turbulent boundary-layer-eddy dynamics. In particular, the secondary instability oscillations result from an inviscidly unstable localized shear layer formed on the interface between a low-speed region and the outer high-speed flow. A qualitatively similar situation exists for the transitional flat-plate boundary layer. Klebanoff *et al.* (1962) showed that a three-dimensional disturbance develops characterized by counter-rotating streamwise vortices. Simultaneously the mean velocity profile became inflexional in the spanwise direction owing to regions of relatively low- and high-speed fluid. Also a localized shear region developed an inflexional velocity profile in the normal direction as measured by Kovasnay *et al.* (1962). This situation was terminated by development of a localized instability in the form of one or more velocity 'spikes' followed by eventual breakdown into turbulence. This behaviour and subsequent oscillations are analogous to the instability oscillations described above for the concave-wall flow. Of course on a flat plate, the Tollmien–Schlichting waves create an unstable flow field for the secondary instability whereas the Görtler instability has no temporal variation. However the timescale of the primary Tollmien–Schlichting instability, namely $3\lambda_{TS}/U_\infty$, is much larger than the timescale of the secondary instability, i.e. $(\partial U/\partial y)^{-1}$, hence the flow is essentially steady. A similar argument holds for the turbulent case below.

In the flat-plate turbulent boundary layer, Kim *et al.* (1971) showed the importance of a localized intermittent instability to the overall bursting sequence during which most of the turbulent production occurs. In their scenario, low-speed streaks slowly moved away from the wall and created instantaneously inflexional velocity profiles. This resulted in oscillatory motions that eventually terminated with a chaotic breakup and production of turbulence. It is interesting to note the similarity between the various oscillatory motions described by Kim *et al.* and those discerned for the concave-wall flow. They observed three oscillatory motions in the form of a growing streamwise vortex, a transverse vortex, and a wavy motion in the (x, z)- and (x, y)-planes. The latter two are respectively qualitatively similar to the horseshoe vortex and sinuous lateral motions observed in figure 14. (The transverse vortex motion would correspond to the apparent vortex train on the plane of symmetry of the horseshoe-vortex series in figure 14.) The wavy motion was found by Kim *et al.* to be the more common of the two, in agreement with our results.

Obviously transitional and turbulent boundary layers have many similarities to which the present results may be applicable. All of these flows have streamwise vorticity in the wall region (although few direct measurements have been made owing to the lack of a reliable sensor small enough to adequately sample the wall region). In the turbulent case, the vortices have a shorter streamwise length and their origin is unknown. Obviously the large-scale outer eddies, responsible for entrainment in turbulent boundary layers, are missing in the Görtler case. Nevertheless, the dynamics leading to the breakdown of the Görtler vortices appear to be similar to the observations made in turbulent flows. Thus the conclusion that the secondary oscillations are due primarily to $(\partial U/\partial z)$ gradients may be relevant in the turbulent case as well. The numerical data in figure 27 of Moin & Kim (1982) show stronger spanwise gradients than normal ones in the wall region of a turbulent channel flow. Some preliminary work at USC has produced similar results in turbulent boundary layers. These results suggest that manipulating the spanwise velocity gradient in flow fields with streamwise vorticity may be an effective control mechanism for altering

their development. The riblets utilized by Walsh (1980) to reduce the drag on a flat plate possibly accomplished this by decreasing the $(\partial U/\partial z)$ gradients. Other novel techniques for controlling the drag and turbulent energy production may also be developed by exploiting these results.

The authors gratefully acknowledge the help of Professor J. H. Haritonidis in the implementation of the Burg spectral-analysis technique and construction of the hot-wire rakes. Mr Roy Myose was very helpful in the programming of the contour plotting routines. Appreciation is also extended to Professors Frederick Browand and Richard Kaplan for their helpful comments regarding this work. This work was sponsored by the Air Force Office of Scientific Research under contract F49620-78-C-0060. The original construction of the facilities used in this study was provided for by NASA Langley Research Center through grant NAG1-19. The most generous support of both these organizations is greatly appreciated.

REFERENCES

ANDERSEN, N. 1974 *Geophys.* **39**, 69.

AIHARA, Y. & KOYAMA, H. 1981 *Trans. Japan Soc. Aeron. Space Sci.* **24**, 78.

AIHARA, Y. & SONODA, T. 1981 *AIAA Paper* 81-0197.

BAKEWELL, H. P. & LUMLEY, J. L. 1967 *Phys. Fluids* **10**, 1880.

BIPPES, H. 1972 *Heidel. Akad. Wiss., Naturwiss. Kl., Sitzungsber.* **3**, 103.

BLACKWELDER, R. F. 1983 *Phys. Fluids* **26**, 2807.

BLACKWELDER, R. F. & ECKELMANN, H. 1979 *J. Fluid Mech.* **94**, 577.

BLACKWELDER, R. F. & HARITONIDIS, J. H. 1983 *J. Fluid Mech.* **132**, 87.

BLACKWELDER, R. F. & KAPLAN, R. E. 1976 *J. Fluid Mech.* **76**, 89.

BROWN, G. L. & THOMAS, A. S. W. 1977 *Phys. Fluids Suppl.* **20**, S243.

BURG, J. P. 1967 Maximum entropy spectral analysis. *Presented at the 37th Annual Intl Meeting, Society of Exploration Geophysicists, Oklahoma City, Oklahoma, 31 October 1967.*

CANTWELL, B. J., COLES, D. E. & DIMOTAKIS, P. E. 1978 *J. Fluid Mech.* **87**, 641.

COLES, D. 1965 *J. Fluid Mech.* **21**, 385.

CORINO, E. R. & BRODKEY, R. S. 1969 *J. Fluid Mech.* **37**, 1.

CORKE, T., KOGA, D., DRUBKA, R. & NAGIB, H. 1980 In *Proc. ICIASF, IEEE Publication* 77CH1251-8 AES, p. 74.

DRYDEN, H. L. 1948 In *Adv. Appl. Mech. I.*, p. 1. Academic Press.

FLORYAN, J. M. & SARIC, W. S. 1982 *AIAA J.* **20**, 316.

GÖRTLER, H. 1940 *Nachr. Wiss. Ges. Göttingen Math.-Phys. Kl.* **2**, 1.

GRASS, A. J. 1971 *J. Fluid Mech.* **50**, 233.

HALL, P. 1983 *J. Fluid Mech.* **130**, 41.

HÄMMERLIN, G. 1955 *J. Rat. Mech. Anal.* **4**, 279.

HARITONIDIS, J. H. 1978 On the wave packets and streaks associated with the transitional spot. Ph.D. dissertation, University of Southern California.

JEANS, A. H. & JOHNSTON, J. P. 1983 *Stanford University Rep.* MD-40.

KIM, H. T., KLINE, S. J. & REYNOLDS, W. C. 1971 *J. Fluid Mech.* **50**, 133.

KLEBANOFF, P. S., TIDSTROM, K. D. & SARGENT, L. M. 1962 *J. Fluid Mech.* **12**, 1.

KLINE, S. J., REYNOLDS, W. C., SCHRAUB, F. A. & RUNSTADLER, P. W. 1967 *J. Fluid Mech.* **30**, 741.

KOMODA, H. 1967 *Phys. Fluids Suppl.* **10**, S87.

KOVASNAY, L. S. G., KOMODA, H. & VASUDEVA, B. R. 1962 In *Proc. Heat Transfer and Fluid Mech. Inst.*, p. 1. Stanford University Press.

LIEPMANN, H. W. 1945 *NACA Wartime Rep.* W-87.

MATTINGLY, G. E. & CRIMINALE, W. O. 1972 *J. Fluid Mech.* **51**, 233.

MICHALKE, A. 1965 *J. Fluid Mech.* **23**, 521.

MOIN, P. & KIM, J. 1982 *J. Fluid Mech.* **118**, 341.

MORKOVIN, M. V. 1979 *NASA Contractor Rep.* 159061.

NISHIOKA, M. & ASAI, M. 1984 In *Turbulence and Chaotic Phenomena in Fluids* (ed. T. Tatsumi), p. 87. Elsevier.

NISHIOKA, M., ASAI, M. & IIDA, S. 1980 In *Laminar–Turbulent Transition* (ed. R. Eppler & H. Fasel), p. 37. Springer.

SATO, H. & KURIKI, K. 1961 *J. Fluid Mech.* **11**, 321.

SMITH, A. M. O. 1955 *Q. Appl. Maths* **13**, 233.

SMITH, C. R. 1984 In *Proc. Eighth Symp. on Turbulence* (ed. G. K. Patterson & J. L. Zakin), Dept. of Chem. Engng, University of Missouri-Rolla.

SMITH, C. R. & ABBOTT, D. E. (eds) 1979 *Coherent Structures of Turbulent Boundary Layers.* Leheigh University.

SMITH, C. R. & SCHWARTZ, S. P. 1983 *Phys. Fluids* **26**, 641.

SWEARINGEN, J. D. & BLACKWELDER, R. F. 1986 *AIAA J.* **24**, 1706.

TANI, I. 1962 *J. Geophys. Res.* **67**, 3075.

TANI, I. & SAKAGAMI, J. 1962 In *Proc. Intl Council of the Aerospace Sciences, Stockholm* (ed. M. Roy), p. 391. Spartan.

WALSH, M. J. 1982 *Prog. Astronaut. Aero.* **72**, 168.

WHITE, F. M. 1974 *Viscous Fluid Flow.* McGraw-Hill.

WINOTO, S. H. & CRANE, R. I. 1980 *Intl J. Heat and Fluid Flow* **2**, 221.

WYGNANSKI, I., HARITONIDIS, J. H. & KAPLAN, R. E. 1979 *J. Fluid Mech.* **92**, 505.